

Supporting Information:

High-throughput computation and machine learning screening of van der Waals heterostructures for Z-scheme photocatalysis

Xiaoqing Liu,^{a,b¶} Yifan Li^{a¶}, Xiuying Zhang^a, Yi-ming Zhao^a, Xian Wang^c, Jun Zhou^d,
Jiadong Shen^a, Miao Zhou^{b*}, Lei Shen^{a*}

^a *Department of Mechanical Engineering, National University of Singapore, Singapore 117575.*

^b *Key Laboratory of Optoelectronic Technology and System of Ministry of Education, College of Optoelectronic Engineering, Chongqing University, Chongqing, 400044, P. R. China*

^c *Department of Physics, National University of Singapore, 2 Science Drive 3, Singapore 117542, Singapore.*

^d *Institute of Materials Research and Engineering (IMRE), Agency for Science, Technology and Research (A*STAR), 2 Fusionopolis Way, Innovis #08-03, Singapore 138634, Republic of Singapore*

*Corresponding author.

E-mail address: mzhou@cqu.edu.cn (M. Zhou).

*Corresponding author.

E-mail address: shenlei@nus.edu.sg (L. Shen).

Text S1. To accurately study and predict the heterostructure type of 2D materials, it is crucial to analyze their fundamental properties comprehensively. Therefore, in this study, we systematically calculated and analyzed the geometric structure, electronic structure, and magnetic properties of 155 2D materials obtained from the 2Dmatpedia database.¹ In Data S1, we present the calculated data obtained from our analyses of the 155 2D materials, including their lattice parameters, HSE band gap, gap type, conduction band minimum (CBM), and valence band maximum (VBM) positions relative to the vacuum level.

Text S2. The method to calculate the Allen materials electronegativity.

To predict the charge transfer direction of the heterostructure and identify whether it is of the Z-scheme type, we propose using the Allen materials electronegativity (χ_m) based on the Allen element electronegativity (χ_e).²⁻⁴ The Allen element electronegativity is primarily based on the average energy of the valence electrons in free atoms. Using Allen electronegativity is based on the principle that energy tends to be transferred from high to low, including the energy of valence electrons. The χ_m is calculated using a modified version of the Allen element electronegativity formula as expressed,⁵

$$\chi_m = \frac{\sum_{i=element} x_i (n_{si} \epsilon_{si} + n_{pi} \epsilon_{pi} + n_{di} \epsilon_{di})}{\sum_{i=element} x_i (n_{si} + n_{pi} + n_{di})},$$

where, $\epsilon_{si,pi,di}$ are the one-electron energies of s-, p- and d-electrons in the free atom of i element, and $n_{si,pi,di}$ are the number of s-, p- and d-electrons in the valence shell. X_i is the number of elements in the chemical formulas. The one-electron energies can be determined directly from spectroscopic data. The necessary data are available for almost all elements, and this method allows the estimation of electronegativities for elements that the other methods cannot treat. All data relating to the calculation of Allen

material electronegativity can be found in Data S2 and S3. Data S2 includes the element and the number of s-, p-, and d-electrons in the valence shell. Data S3 includes one-electron energies of s-, p-, and d-electrons in the free atom of various elements obtained from the website (<http://www.graylark.com/eve/orbital-energies-table.html>). Noted: Electronvolts (eV) (the most appropriate units; Rydberg to eV conversion factor = 13.6058^3) and Pauling units (Rydberg to PU conversion factor = 2.3^6)

Text S3 The detail of relationship of these two descriptors in affecting interfacial charge transfer

We also employed the reinforcement learning-based Physio symbolic regression package,⁷ which leverages physical unit constraints for the analytical inference of physical laws. A simple analytical model for the charge transfer and descriptors was rigorously derived by inputting parameters. This approach complements the DFT calculations by providing an analytical model for understanding the fundamental interactions captured in the simulations. A dataset of 35 data points was used for training, and 10 data points for testing. Training was conducted using the Φ -SO algorithm, which incorporates physical unit constraints during symbolic expression generation. Candidate expressions were evaluated based on mean squared error (MSE), unit consistency, and symbol complexity. A risk-seeking policy gradient strategy was applied, rewarding only the top 5% of candidates. Key hyperparameters included a batch size of 100, learning rate of 0.0025, and entropy coefficient of 0.05. After training, Φ -SO derived a concise, accurate expression, demonstrating strong performance even on small datasets.

Text S4 Computational details of machine learning and screening criteria

Machine Learning Model Setup

For both machine learning E2E FFN classification and linear regression models, all input features were standardized to have a mean of 0 and a standard deviation of 1, eliminating scale differences and facilitating enhanced convergence during model training.⁸

E2E FFN classification model

A fully connected neural network (FCNN) was constructed for binary classification, comprising an input layer, three hidden layers, and an output layer. The input layer size corresponded to the number of input features, while the hidden layers contained 128, 64, and 32 neurons, respectively, with ReLU activation functions. To prevent overfitting, dropout regularization (rate = 20%) was applied after each hidden layer. The output layer consisted of a single neuron with a sigmoid activation function to predict class probabilities.^{9, 10} The Adam optimizer¹¹ (learning rate = 0.001) and binary cross-entropy loss were employed,¹² with early stopping based on validation loss to avoid overfitting. It was trained for 50 epochs with a batch size of 32, utilizing 5-fold cross-validation to ensure robust evaluation. Model performance was assessed using accuracy, precision, recall, and F1 score. The final model achieved high classification accuracy on the validation set, and predictions on the test set were saved for subsequent analysis.

E2E FFN linear regression model

Structural features of the materials were extracted from CIF files using pymatgen, including volume, density, lattice constants (a, b, c), lattice angles (α , β , γ), and space group numbers.^{13, 14} These features were used to build a fully connected neural network (FCNN) for regression to predict electronic properties such as the CBM, VBM, and band gap. The FCNN comprised three hidden layers with 128, 64, and 32 neurons, respectively, each employing ReLU activation functions. To prevent overfitting, dropout regularization with a rate of 20% was applied after each hidden layer. The output layer utilized a linear activation function to predict the target electronic properties.^{10, 15} The model was trained using the Adam optimizer¹¹ with a learning rate of 0.001 and a custom physics-guided loss function combining mean squared error (MSE) and physical constraints.¹⁶ This loss function was designed as follows:

$$L = \alpha \cdot MSE + \beta \cdot L_{phy}$$

where α and β are weighting coefficients and L_{phy} represents specific constraints (Band gap values constrained by CBM-VBM).

Training was performed using 80% of the data, with the remaining 20% reserved for validation. Model performance was evaluated using mean absolute error (MAE=0.079)

and R^2 scores (0.939).¹⁷ The trained model was then tested on unseen data, and predictions were saved for further analysis.

Post-machine learning screening of band edge predictions

The following criteria were applied to the predicted band edges to ensure optimal photocatalytic performance:

1. Band Gap (A or B) < 2 eV: Band gaps below 2 eV enhance visible light absorption, which is critical for photocatalytic water splitting¹⁸. This ensures at least one of the materials in the heterojunction possesses an appropriate band gap for efficient absorption of visible light.
2. Heterojunction Band Gap < 0.5 eV: A heterojunction band gap less than 0.5 eV facilitates efficient charge transfer between materials, enhancing the separation of photogenerated electron-hole pairs and minimizing recombination losses via the Z-scheme mechanism¹⁹.
3. Photogenerated Potential ($\chi(\text{H}_2) > 1 \text{ eV}$ and $\chi(\text{O}_2) > 1 \text{ eV}$): A photogenerated potential exceeding 1 eV for hydrogen evolution reaction (HER) and oxygen evolution reaction (OER) ensures that the heterojunction generates sufficient photovoltage to drive water splitting reactions efficiently²⁰.
4. Charge Redistribution ($\Delta Q > 0.1$): A ΔQ value exceeding 0.1 indicates sufficient charge redistribution at the heterojunction interface, promoting charge separation, reducing electron-hole recombination, and thereby improving photocatalytic performance²¹.

Table S1. Heterostructures predict Z-scheme using ΔV (eV) and $\Delta\chi_m$, with a test range from 0 to 1.0 eV and 0 to 0.2, respectively.

| Predict Type (Z-scheme) | $\Delta\chi_m > 0.00$ | $\Delta\chi_m > 0.05$ | $\Delta\chi_m > 0.10$ | $\Delta\chi_m > 0.20$ | $\Delta\chi_m > 0.20$ |
|-------------------------|-----------------------|-----------------------|-----------------------|-----------------------|-----------------------|
| $\Delta V > 0$ | 1863 | 1784 | 1684 | 1549 | 1496 |
| $\Delta V > 0.2$ | 1622 | 1559 | 1481 | 1365 | 1321 |
| $\Delta V > 0.4$ | 1389 | 1338 | 1269 | 1170 | 1130 |
| $\Delta V > 0.6$ | 1160 | 1118 | 1062 | 987 | 959 |
| $\Delta V > 0.8$ | 941 | 905 | 858 | 803 | 778 |
| $\Delta V > 1.0$ | 785 | 757 | 714 | 670 | 652 |

Table S2. Heterostructures with HSE calculation, including atoms, lattice ((Å)), lattice mismatch (δ) (%), interlayer distance (Δd) (Å), and binding energy (E_b) (meV per atom).

| serial number | Acceptor/donor | Ato ms | lattice | δ | Δd | E_b |
|---------------|--|--------|---------------|----------|------------|--------|
| 1 | SnO ₂ /GaN | 5 | a=b=3.24 | 0.61% | 2.81 | -44.70 |
| 2 | SbBrO/CuI | 10 | a=b=3.91 | 4.60% | 3.83 | -18.39 |
| 3 | CuClO ₂ /TeRhCl | 14 | a=3.68,b=6.73 | 2.28% | 2.90 | -32.11 |
| 4 | HfS ₂ /Te ₂ W | 6 | a=b=3.62 | 3.07% | 3.48 | -37.57 |
| 5 | AuClO ₂ /TaI ₂ O | 16 | a=3.90,b=7.44 | 0.20% | 3.21 | -23.28 |
| 6 | PdCl ₂ /SnSe | 10 | a=4.00,b=9.43 | 0.13% | 2.67 | -54.28 |
| 7 | SnS ₂ /Te ₂ Mo | 6 | a=b=3.65 | 4.33% | 3.38 | -37.82 |
| 8 | Bi ₂ Te ₂ Se/Sr(SnAs) | | a=b=4.32 | 3.48% | 2.69 | -38.88 |
| | 2 | 10 | | | | |
| 9 | SnSe ₂ /Te ₃ As ₂ | 8 | a=b=4.03 | 4.58% | 2.99 | -37.44 |
| 10 | AuO ₂ F/HfTeSe ₄ | 14 | a=3.87,b=6.92 | 0.56% | 2.80 | -31.62 |
| 11 | Bi ₂ TeSe ₂ /Sb | 7 | a=b=4.25 | 2.64% | 3.13 | -38.93 |
| 12 | NiS ₂ /MoSe ₂ | 6 | a=b=3.35 | 0.83% | 3.25 | -33.67 |
| 13 | SnO ₂ /WSe ₂ | 6 | a=b=3.29 | 2.14% | 3.02 | -34.43 |
| 14 | SnO ₂ /ZnO | 5 | a=b=3.28 | 1.96% | 2.60 | -52.49 |
| 15 | PtO ₂ /MoSe ₂ | 6 | a=b=3.25 | 4.54% | 2.89 | -36.35 |
| 16 | AuBrO ₂ /TaI ₂ O | 8 | a=3.86,b=7.48 | 0.92% | 3.81 | -36.76 |
| 17 | AuO ₂ F/TeRhCl | 14 | a=3.73,b=6.85 | 4.12% | 2.84 | -32.81 |
| 18 | Bi ₂ Se ₃ /GaGeTe | 11 | a=b=4.17 | 1.27% | 3.12 | -24.56 |
| 19 | Bi ₂ Se ₃ /GaTe | 9 | a=b=4.18 | 0.86% | 3.24 | -29.54 |
| 20 | Bi ₂ Se ₃ /Mn(BiTe ₂) ₂ | 12 | a=b=4.28 | 3.64% | 3.82 | -17.69 |
| 21 | Bi ₂ Se ₃ /VI ₂ | 8 | a=b=4.18 | 1.49% | 3.33 | -31.09 |
| 22 | Bi ₂ Te ₂ S/AuI | 9 | a=b=4.27 | 0.48% | 3.00 | -34.78 |
| 23 | BiBrO/CuI | 10 | a=b=3.99 | 1.62% | 3.91 | -17.27 |
| 24 | BiIO/CuI | 10 | a=b=4.06 | 0.48% | 3.17 | -27.66 |
| 25 | BiClO/CuI | 10 | a=b=3.95 | 2.78% | 3.80 | -17.25 |
| 26 | SnO ₂ /MoSe ₂ | 6 | a=b=3.29 | 2.14% | 2.93 | -34.70 |
| 27 | NiS ₂ /WSe ₂ | 6 | a=b=3.35 | 0.83% | 3.25 | -34.34 |
| 28 | Bi ₂ Se ₃ /Sb | 7 | a=b=4.19 | 0.68% | 3.16 | -38.67 |
| 29 | Sb ₂ TeSe ₂ /Sb | 7 | a=b=4.17 | 0.12% | 3.14 | -40.27 |
| 30 | SnS ₂ /As | 5 | a=b=3.69 | 2.08% | 3.12 | -43.06 |
| 31 | Bi ₂ Te ₂ S/Sr(SnAs) ₂ | 10 | a=b=4.26 | 2.55% | 3.18 | -30.66 |
| 32 | HfS ₂ /Te ₂ Mo | 6 | a=b=3.62 | 3.20% | 3.35 | -38.71 |
| 33 | Bi ₂ Se ₃ /Te ₃ As ₂ | 10 | a=b=4.15 | 2.83% | 3.20 | -29.48 |
| 34 | SnO ₂ /WS ₂ | 6 | a=b=3.22 | 1.60% | 2.90 | -32.92 |

Here, the lattice mismatch can be defined by $\delta = (a-b)/b \times 100\%$, where a and b

represent the lattice parameters of the Acceptor and donor, respectively.

(The corresponding binding energy per atom, E_b , was calculated as follows:

$$E_b = \frac{1}{N} [E(\text{heterostructure}) - E(\text{TMDC1}) - E(\text{TMDC2})]$$

where $E(\text{heterostructure})$, $E(\text{TMDC1})$ and $E(\text{TMDC2})$ are the total energy of heterostructure, TMDC1 and TMDC2, respectively. N is the total number of atoms in the supercell.)

Table S3. Heterostructure characters, including HSE06 band gap, the difference of two Allen materials electronegativity, $\Delta\chi_m$, ΔV , the charge transfer from Bader analyst, ΔQ , and verify.

| number | Acceptor/donor | $\Delta\chi_m$ | ΔV (eV) | ΔQ (e) | verify | Ref |
|--------|--|----------------|-----------------|----------------|---------|-------------------|
| 1 | SnO ₂ /GaN | 0.622 | 1.949 | 0.105 | DFT | No |
| 2 | SbBrO/CuI | 0.646 | 1.604 | 0.050 | DFT | No |
| 3 | CuClO ₂ /TeRhCl | 0.775 | 1.557 | 0.241 | DFT | No |
| 4 | HfS ₂ /Te ₂ W | 0.416 | 1.386 | 0.059 | DFT | No |
| 5 | AuClO ₂ /TaI ₂ O | 0.311 | 1.281 | 0.159 | DFT | No |
| 6 | PdCl ₂ /SnSe | 0.132 | 1.085 | 0.288 | DFT | No |
| 7 | SnS ₂ /Te ₂ Mo | 0.533 | 0.972 | 0.055 | DFT | ref ²² |
| 8 | Bi ₂ Te ₂ Se/Sr(SnAs) ₂ | 0.194 | 0.929 | 0.141 | DFT | No |
| 9 | SnSe ₂ /Te ₃ As ₂ | 0.144 | 0.789 | 0.115 | DFT | No |
| 10 | AuO ₂ F/HfTeSe ₄ | 0.899 | 0.767 | 0.128 | DFT | No |
| 11 | Bi ₂ TeSe ₂ /Sb | 0.259 | 2.082 | 0.081 | DFT | No |
| 12 | NiS ₂ /MoSe ₂ | 0.200 | 1.821 | 0.024 | DFT | ref ²³ |
| 13 | SnO ₂ /WSe ₂ | 1.231 | 0.767 | 0.066 | DFT | No |
| 14 | SnO ₂ /ZnO | 0.367 | 1.949 | 0.091 | DFT | ref ²⁴ |
| 15 | PtO ₂ /MoSe ₂ | 0.200 | 1.604 | 0.069 | DFT | ref ²⁵ |
| 16 | AuBrO ₂ /TaI ₂ O | 0.266 | 1.367 | 0.077 | DFT | No |
| 17 | AuO ₂ F/TeRhCl | 1.022 | 0.841 | 0.206 | DFT | No |
| 18 | Bi ₂ Se ₃ /GaGeTe | 0.462 | 0.793 | 0.056 | DFT | No |
| 19 | Bi ₂ Se ₃ /GaTe | 0.147 | 0.637 | 0.043 | DFT | ref ²⁶ |
| 20 | Bi ₂ Se ₃ /Mn(BiTe ₂) ₂ | 0.242 | 0.873 | 0.055 | DFT | No |
| 21 | Bi ₂ Se ₃ /VI ₂ | 0.135 | 1.345 | 0.038 | DFT | No |
| 22 | Bi ₂ Te ₂ S/AuI | 0.105 | 1.126 | -0.022 | Unknown | No |
| 23 | BiBrO/CuI | 0.654 | 1.662 | 0.036 | DFT | ref ²⁷ |
| 24 | BiIO/CuI | 0.518 | 1.557 | 0.012 | DFT | No |
| 25 | BiClO/CuI | 0.735 | 1.288 | 0.044 | DFT | No |
| 26 | SnO ₂ /MoSe ₂ | 1.228 | 1.452 | 0.063 | DFT | No |
| 27 | NiS ₂ /WSe ₂ | 0.203 | 1.397 | 0.031 | DFT | No |
| 28 | Bi ₂ Se ₃ /Sb | 0.323 | 1.306 | 0.081 | DFT | No |
| 29 | Sb ₂ TeSe ₂ /Sb | 0.245 | 0.609 | 0.085 | DFT | No |
| 30 | SnS ₂ /As | 0.261 | 0.646 | 0.050 | DFT | No |
| 31 | Bi ₂ Te ₂ S/Sr(SnAs) ₂ | 0.236 | 1.056 | 0.099 | DFT | No |
| 32 | HfS ₂ /Te ₂ Mo | 0.411 | 1.123 | 0.055 | DFT | ref ²⁸ |
| 33 | Bi ₂ Se ₃ /Te ₃ As ₂ | 0.130 | 0.699 | 0.043 | DFT | No |
| 34 | SnO ₂ /WS ₂ | 1.106 | 1.098 | 0.037 | DFT | No |

Table S4. Heterostructure characters, including HSE06 band gap (E_g), the difference of two Allen materials electronegativity, vacuum level difference ($\Delta\Phi$), photogenerated potentials for HER, $\chi(\text{H}_2)$, and photogenerated potentials for OER, $\chi(\text{O}_2)$. Units are in eV.

| number | Acceptor/donor | E_g | $\Delta\Phi$ | $\chi(\text{H}_2)$ | $\chi(\text{O}_2)$ |
|--------|--|-------|--------------|--------------------|--------------------|
| 1 | SnO ₂ /GaN | 0.06 | 0.574 | 1.815 | 4.021 |
| 2 | SbBrO/CuI | 0.25 | 0.096 | 1.777 | 2.386 |
| 3 | CuClO ₂ /TeRhCl | 0.52 | 0.307 | -0.351 | 2.433 |
| 4 | HfS ₂ /Te ₂ W | 0.11 | 0.102 | 0.308 | 1.177 |
| 5 | AuClO ₂ /TaI ₂ O | 0.29 | 0.247 | 0.270 | 2.350 |
| 6 | PdCl ₂ /SnSe | 0.76 | 0.294 | 0.953 | 2.467 |
| 7 | SnS ₂ /Te ₂ Mo | 0.28 | 0.075 | 0.187 | 1.191 |
| 8 | Bi ₂ Te ₂ Se/Sr(SnAs) ₂ | 0.20 | 0.353 | 0.566 | 0.260 |
| 9 | SnSe ₂ /Te ₃ As ₂ | 0.13 | 0.398 | -0.100 | 1.511 |
| 10 | AuO ₂ F/HfTeSe ₄ | 0.38 | 0.132 | -0.378 | 2.816 |
| 11 | Bi ₂ TeSe ₂ /Sb | 0.68 | 0.155 | 0.652 | 1.081 |
| 12 | NiS ₂ /MoSe ₂ | 0.80 | 0.204 | -0.041 | 0.900 |
| 13 | SnO ₂ /WSe ₂ | 0.19 | 0.282 | 0.510 | 3.913 |
| 14 | SnO ₂ /ZnO | 0.07 | 0.829 | 2.533 | 3.832 |
| 15 | PtO ₂ /MoSe ₂ | 0.49 | 0.267 | 0.282 | 2.822 |
| 16 | AuBrO ₂ /TaI ₂ O | 0.34 | 0.100 | 0.382 | 1.899 |
| 17 | AuO ₂ F/TeRhCl | 0.82 | 0.060 | -0.113 | 2.754 |
| 18 | Bi ₂ Se ₃ /GaGeTe | 0.42 | 0.040 | -0.339 | 1.055 |
| 19 | Bi ₂ Se ₃ /GaTe | 0.71 | 0.030 | 0.476 | 1.107 |
| 20 | Bi ₂ Se ₃ /Mn(BiTe ₂) ₂ | 0.06 | 0.100 | 0.999 | 0.278 |
| 21 | Bi ₂ Se ₃ /VI ₂ | 1.38 | 0.030 | 1.563 | 1.130 |
| 22 | Bi ₂ Te ₂ S/AuI | 1.36 | 0.120 | 1.148 | 0.437 |
| 23 | BiBrO/CuI | 0.69 | 0.120 | 1.756 | 2.741 |
| 24 | BiIO/CuI | 1.00 | 0.020 | 1.844 | 1.620 |
| 25 | BiClO/CuI | 0.83 | 0.050 | 1.771 | 3.063 |
| 26 | SnO ₂ /MoSe ₂ | 0.35 | 0.070 | 0.369 | 4.024 |
| 27 | NiS ₂ /WSe ₂ | 0.56 | 0.090 | 0.476 | 0.846 |
| 28 | Bi ₂ Se ₃ /Sb | 0.53 | 0.030 | 0.787 | 1.117 |
| 29 | Sb ₂ TeSe ₂ /Sb | 0.64 | 0.060 | 1.004 | 0.625 |
| 30 | SnS ₂ /As | 0.86 | 0.030 | 0.641 | 1.996 |
| 31 | Bi ₂ Te ₂ S/Sr(SnAs) ₂ | 0.32 | 0.090 | 0.929 | 0.477 |
| 32 | HfS ₂ /Te ₂ Mo | 0.33 | 0.010 | 0.276 | 1.575 |
| 33 | Bi ₂ Se ₃ /Te ₃ As ₂ | 0.51 | 0.060 | -0.183 | 1.029 |
| 34 | SnO ₂ /WS ₂ | 0.91 | 0.060 | 0.096 | 4.295 |

Table S5. Heterostructure characters by Machine learning, including ML predicted band gap (E_g), ML predicted the charge transfer from Bader analyst, ΔQ , ML predicted photogenerated potentials for HER, $\chi(H_2)$, and ML predicted photogenerated potentials for OER, $\chi(O_2)$. Units are in eV.

| number | A/B | E_g | ΔQ | $\chi(H_2)$ | $\chi(O_2)$ |
|--------|--|-------|------------|-------------|-------------|
| 1 | AgI/AuClO ₂ | 0.28 | -0.38 | 1.10 | 2.48 |
| 2 | AgI/TiNCl | 0.41 | -0.29 | 1.19 | 1.33 |
| 3 | AuBr/AuBrO ₂ | 0.10 | -0.52 | 1.13 | 2.11 |
| 4 | AuBr/TiNCl | 0.05 | -0.51 | 1.05 | 1.42 |
| 5 | AuBrO ₂ /CuI(2dm-3638) | 0.46 | 1.59 | 1.59 | 1.72 |
| 6 | AuClO ₂ /Al ₂ ZnS ₄ | 0.27 | 0.55 | 1.36 | 2.03 |
| 7 | AuClO ₂ /Ba(BSe ₃) ₂ | 0.40 | 0.93 | 1.55 | 2.11 |
| 8 | AuClO ₂ /GaN | 0.10 | 0.22 | 1.66 | 1.62 |
| 9 | Ba(BSe ₃) ₂ /AuBrO ₂ | 0.04 | -0.72 | 1.22 | 2.23 |
| 10 | Ba(BSe ₃) ₂ /TiBrN | 0.05 | -0.34 | 1.25 | 1.39 |
| 11 | Ba(BSe ₃) ₂ /TiNCl | 0.09 | -0.61 | 1.26 | 1.44 |
| 12 | Br/AuI | 0.15 | 0.57 | 1.28 | 1.94 |
| 13 | Br/Ba(BSe ₃) ₂ | 0.42 | 0.22 | 1.61 | 1.99 |
| 14 | Br/CuI(2dm-4972) | 0.19 | 0.66 | 1.59 | 1.93 |
| 15 | CuBr/AuBrO ₂ | 0.13 | -0.22 | 1.04 | 2.14 |
| 16 | CuI(2dm-3638)/TiBrN | 0.04 | -0.89 | 1.11 | 1.56 |
| 17 | CuI(2dm-4972)/AuBrO ₂ | 0.05 | -1.57 | 1.08 | 2.23 |
| 18 | LiCuO ₂ /CuBiO ₂ | 0.13 | 0.18 | 1.40 | 1.35 |
| 19 | LiCuO ₂ /KH ₂ N | 0.12 | 0.88 | 1.48 | 1.63 |
| 20 | MnI ₂ /AuBrO ₂ | 0.16 | -0.29 | 1.12 | 2.09 |
| 21 | PdCl ₂ /AuI(2dm-3495) | 0.39 | 0.26 | 1.18 | 1.25 |
| 22 | PdCl ₂ /CuI(2dm-3638) | 0.49 | 0.18 | 1.64 | 1.25 |
| 23 | PdCl ₂ /CuI(2dm-4972) | 0.49 | 0.18 | 1.46 | 1.25 |
| 24 | SnS/AuBrO ₂ | 0.07 | -0.82 | 1.07 | 2.19 |
| 25 | SnS/TiBrN | 0.07 | -0.38 | 1.10 | 1.54 |
| 26 | TiNF/AgBiO ₂ | 0.41 | 1.13 | 1.42 | 1.46 |
| 27 | VI ₂ /TiBrN | 0.06 | -0.55 | 1.58 | 1.31 |
| 28 | VI ₂ /TiNCl | 0.04 | -0.88 | 1.18 | 1.38 |
| 29 | WF ₅ /GaN | 0.25 | 2.65 | 1.59 | 2.34 |

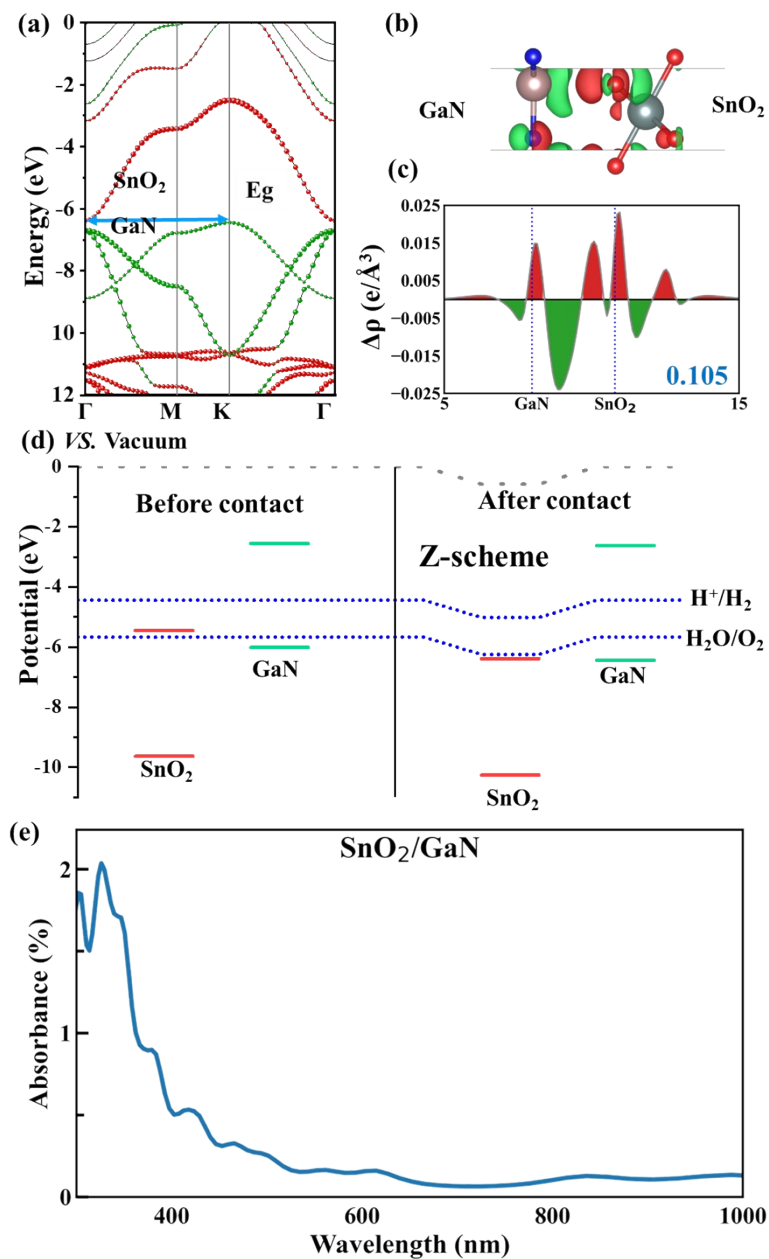


Figure S1. The electronic structures of SnO₂/GaN were calculated, encompassing (a) HSE band structures, (b) charge transfer difference, (c) plane-integrated electron density difference along the vertical direction, (d) band alignment, and (e) absorption coefficients. The red and blue regions indicate electron accumulation and depletion, respectively. The isosurface value is $\pm 0.0005 \text{ e}\text{\AA}^{-3}$. The number labeled in blue is the amount of the interlayer charge transfer (in e) calculated by the Bader charge analysis.

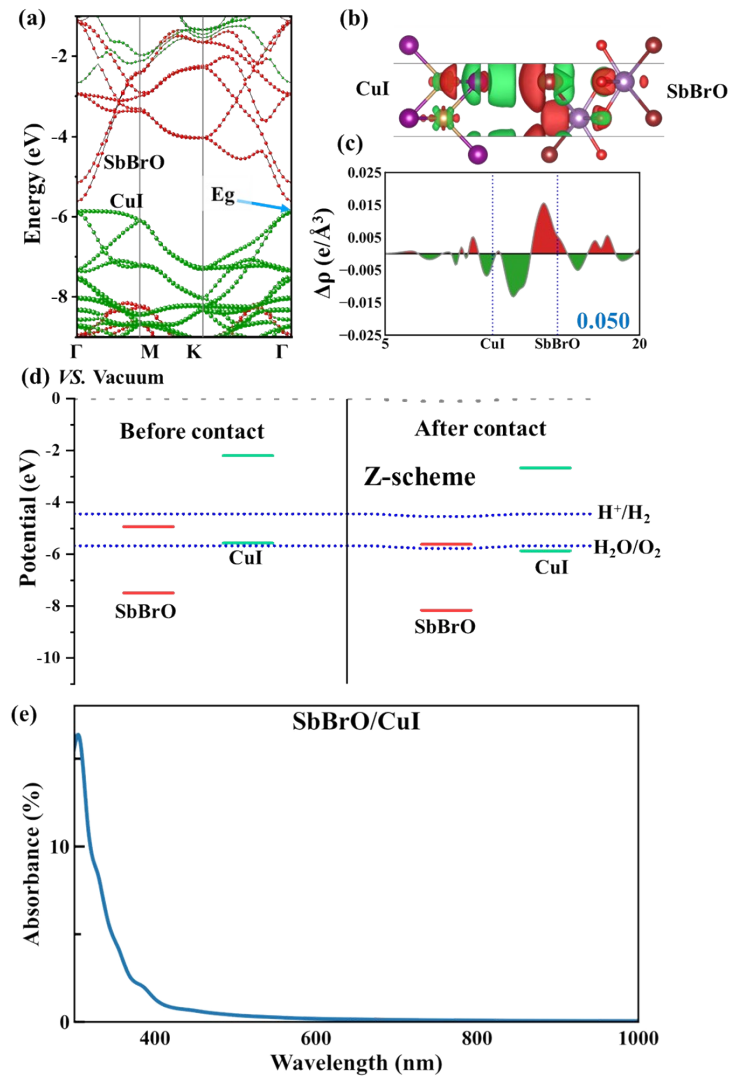


Figure S2. The electronic structures of SbBrO/CuI were calculated, encompassing (a) HSE band structures, (b) charge transfer difference, (c) plane-integrated electron density difference along the vertical direction, (d) band alignment, and (e) absorption coefficients. The red and blue regions indicate electron accumulation and depletion, respectively. The isosurface value is $\pm 0.0001 \text{ e \AA}^{-3}$. The number labeled in blue is the amount of the interlayer charge transfer (in e) calculated by the Bader charge analysis.

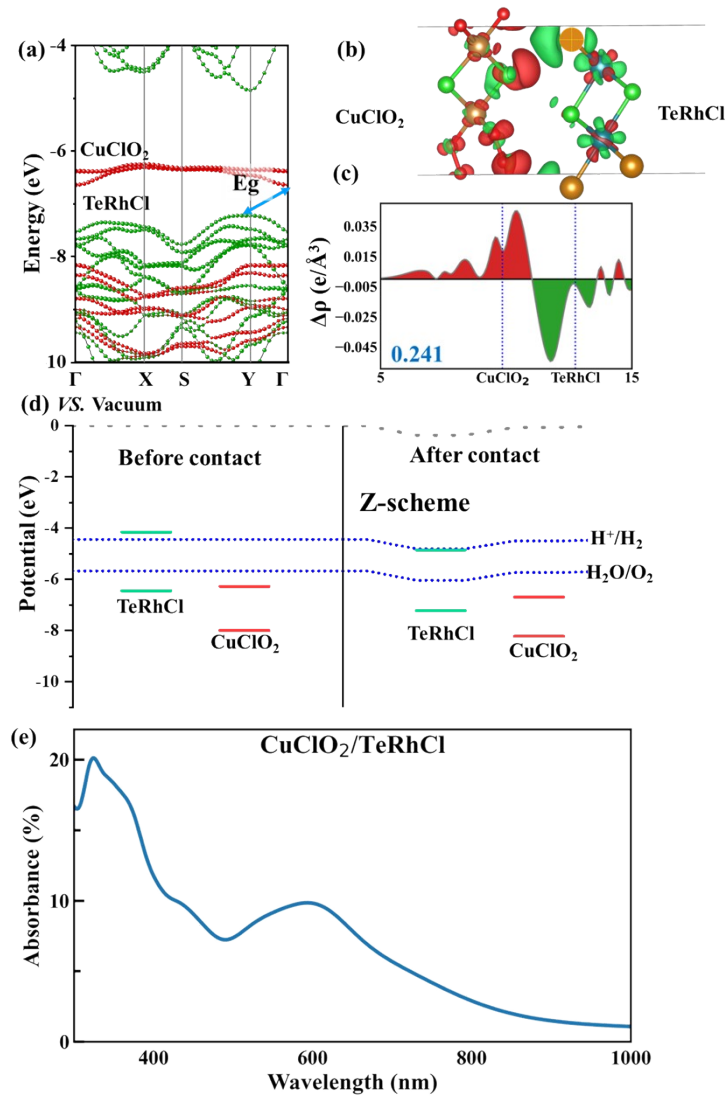


Figure S3. The electronic structures of $\text{CuClO}_2/\text{TeRhCl}$ were calculated, encompassing (a) HSE band structures, (b) charge transfer difference, (c) plane-integrated electron density difference along the vertical direction, (d) band alignment, and (e) absorption coefficients. The red and blue regions indicate electron accumulation and depletion, respectively. The isosurface value is $\pm 0.0005 \text{ e \AA}^{-3}$. The number labeled in blue is the amount of the interlayer charge transfer (in e) calculated by the Bader charge analysis.

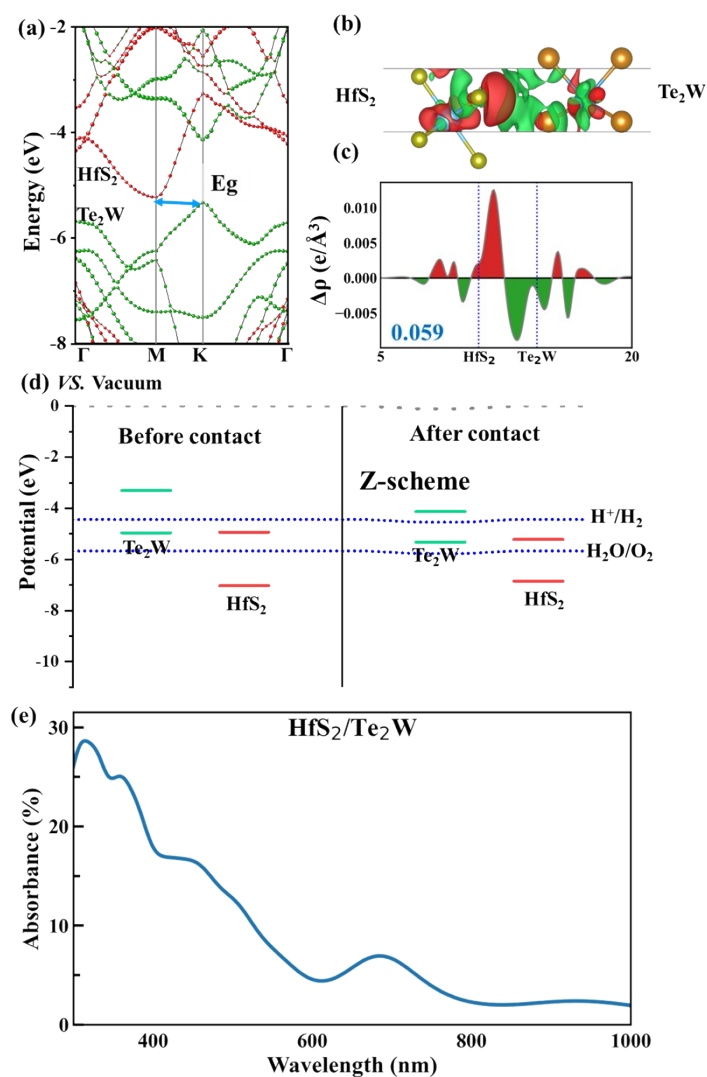


Figure S4. The electronic structures of $\text{HfS}_2/\text{Te}_2\text{W}$ were calculated, encompassing (a) HSE band structures, (b) charge transfer difference, (c) plane-integrated electron density difference along the vertical direction, (d) band alignment, and (e) absorption coefficients. The red and blue regions indicate electron accumulation and depletion, respectively. The isosurface value is $\pm 0.0001 \text{ e } \text{\AA}^{-3}$. The number labeled in blue is the amount of the interlayer charge transfer (in e) calculated by the Bader charge analysis.

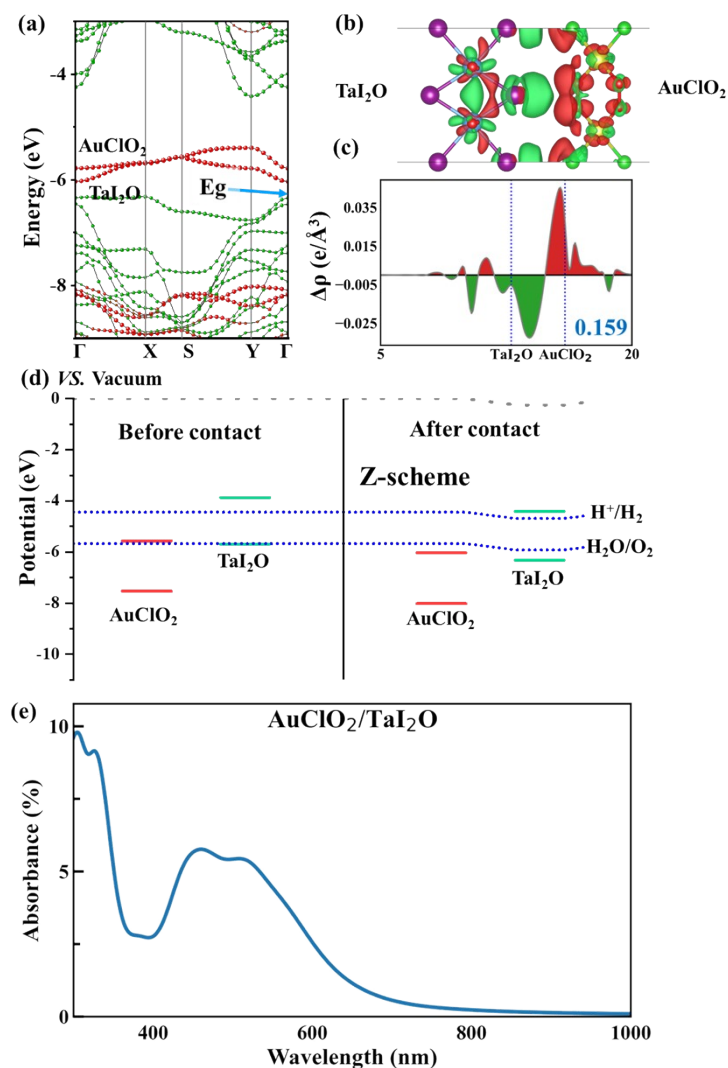


Figure S5. The electronic structures of $\text{AuClO}_2/\text{TaI}_2\text{O}$ were calculated, encompassing (a) HSE band structures, (b) charge transfer difference, (c) plane-integrated electron density difference along the vertical direction, (d) band alignment, and (e) absorption coefficients. The red and blue regions indicate electron accumulation and depletion, respectively. The isosurface value is $\pm 0.0002 \text{ e \AA}^{-3}$. The number labeled in blue is the amount of the interlayer charge transfer (in e) calculated by the Bader charge analysis.

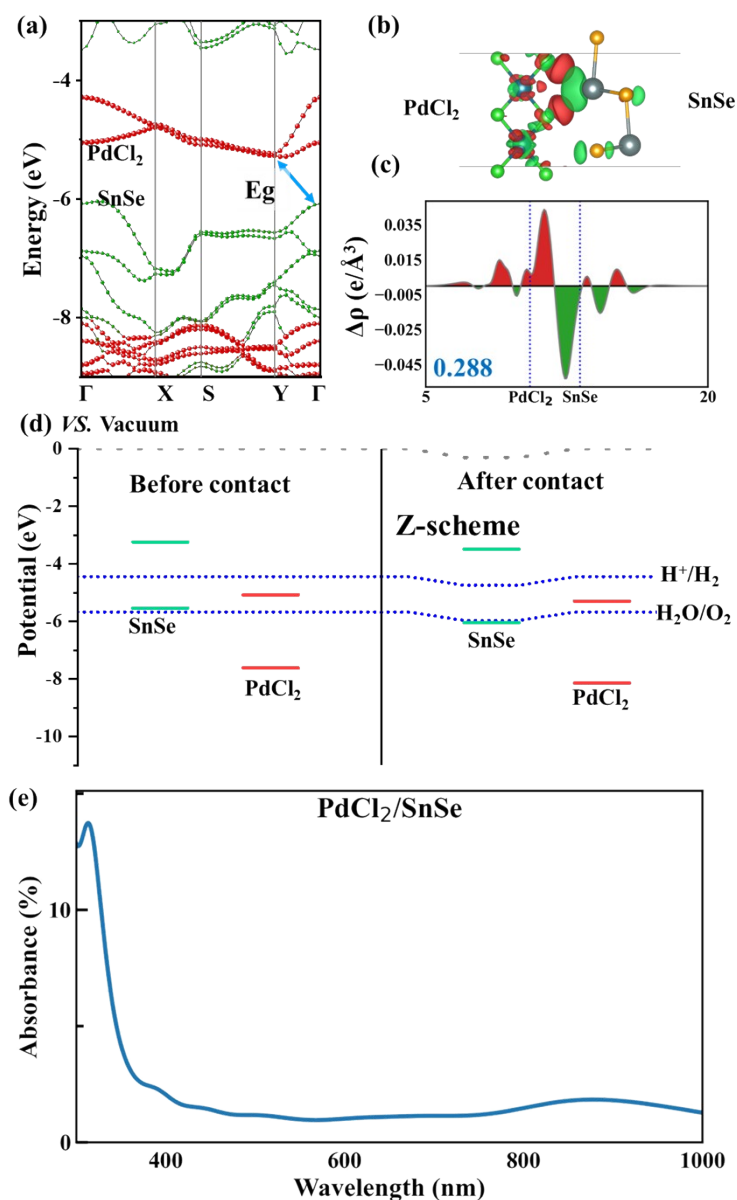


Figure S6. The electronic structures of PdCl₂/SnSe were calculated, encompassing (a) HSE band structures, (b) charge transfer difference, (c) plane-integrated electron density difference along the vertical direction, (d) band alignment, and (e) absorption coefficients. The red and blue regions indicate electron accumulation and depletion, respectively. The isosurface value is $\pm 0.0005 \text{ e \AA}^{-3}$. The number labeled in blue is the amount of the interlayer charge transfer (in e) calculated by the Bader charge analysis.

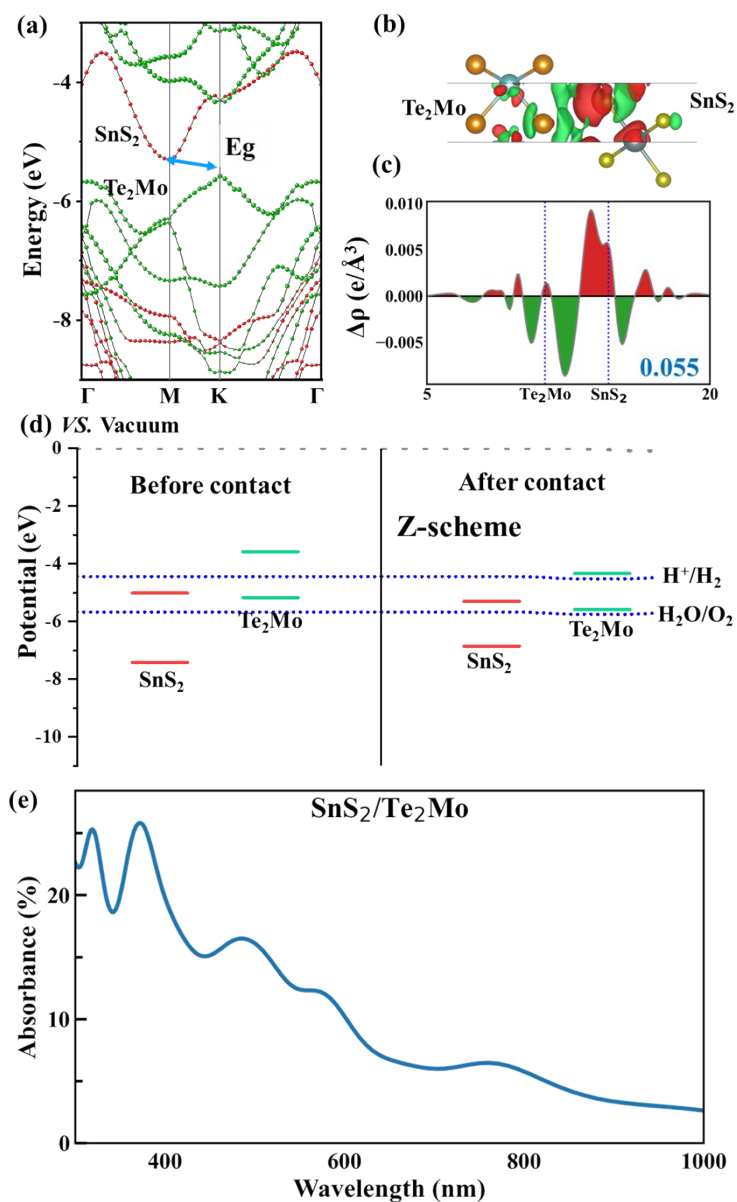


Figure S7. The electronic structures of SnS₂/Te₂Mo were calculated, encompassing (a) HSE band structures, (b) charge transfer difference, (c) plane-integrated electron density difference along the vertical direction, (d) band alignment, and (e) absorption coefficients. The red and blue regions indicate electron accumulation and depletion, respectively. The isosurface value is $\pm 0.0001 \text{ e \AA}^{-3}$. The number labeled in blue is the amount of the interlayer charge transfer (in e) calculated by the Bader charge analysis.

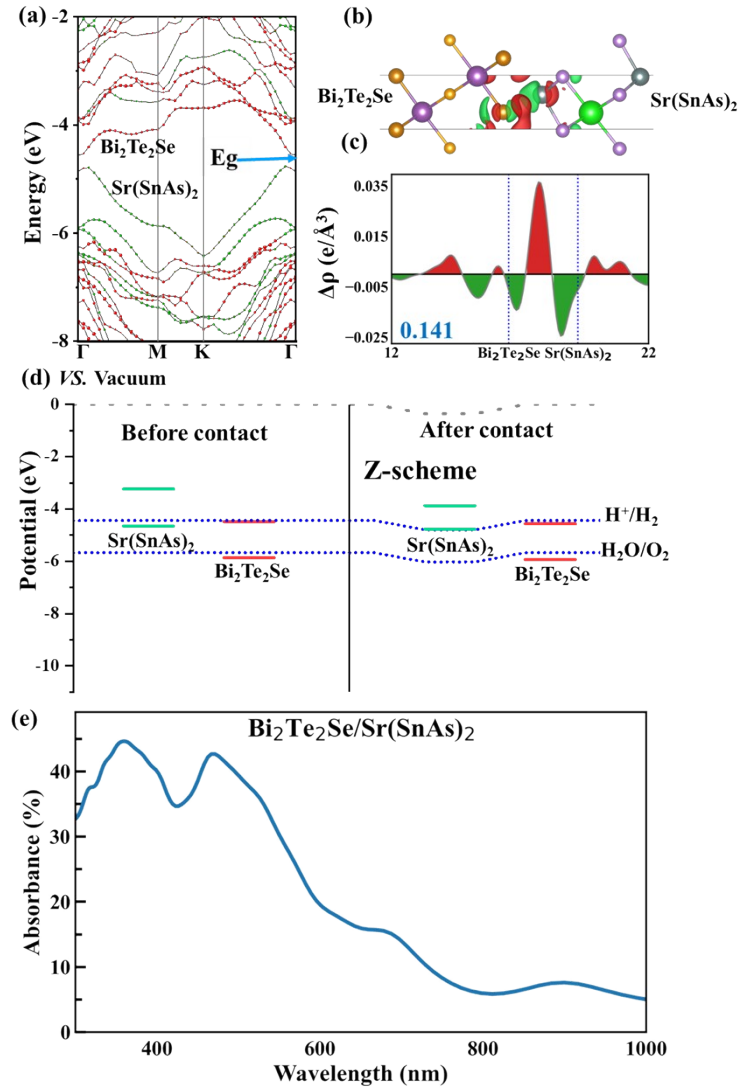


Figure S8. The electronic structures of $\text{Bi}_2\text{Te}_2\text{Se}/\text{Sr}(\text{SnAs})_2$ were calculated, encompassing (a) HSE band structures, (b) charge transfer difference, (c) plane-integrated electron density difference along the vertical direction, (d) band alignment, and (e) absorption coefficients. The red and blue regions indicate electron accumulation and depletion, respectively. The isosurface value is $\pm 0.0005 \text{ e } \text{\AA}^{-3}$. The number labeled in blue is the amount of the interlayer charge transfer (in e) calculated by the Bader charge analysis.

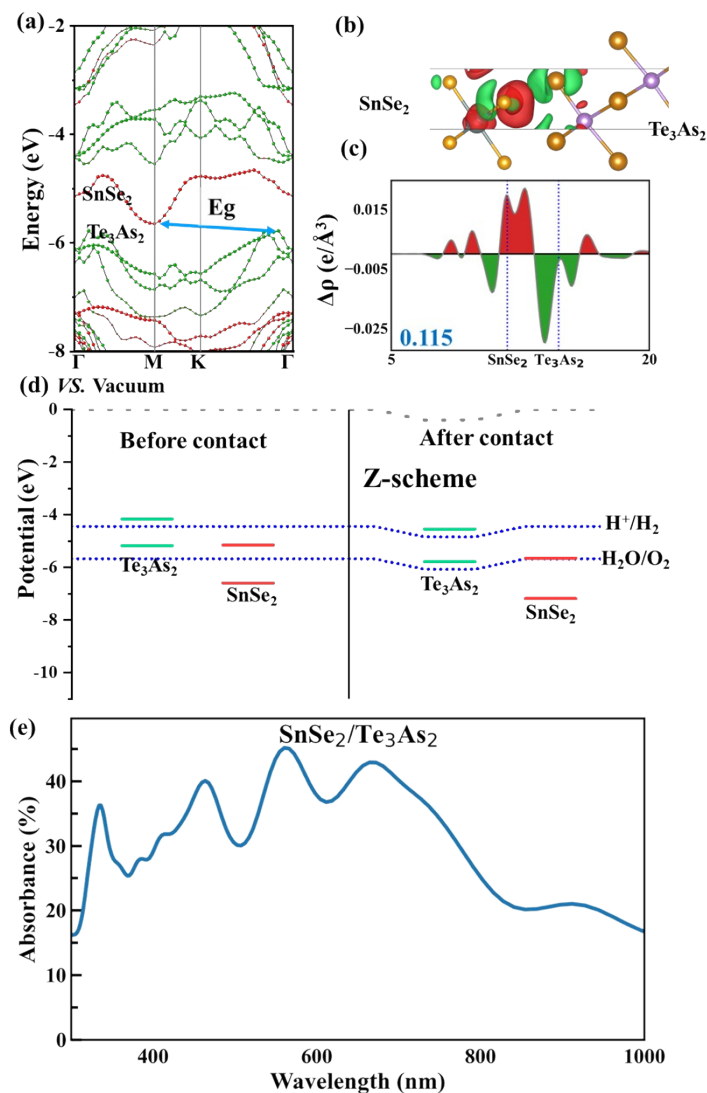


Figure S9. The electronic structures of $\text{SnSe}_2/\text{Te}_3\text{As}_2$ were calculated, encompassing (a) HSE band structures, (b) charge transfer difference, (c) plane-integrated electron density difference along the vertical direction, (d) band alignment, and (e) absorption coefficients. The red and blue regions indicate electron accumulation and depletion, respectively. The isosurface value is $\pm 0.0003 \text{ e}\text{\AA}^{-3}$. The number labeled in blue is the amount of the interlayer charge transfer (in e) calculated by the Bader charge analysis.

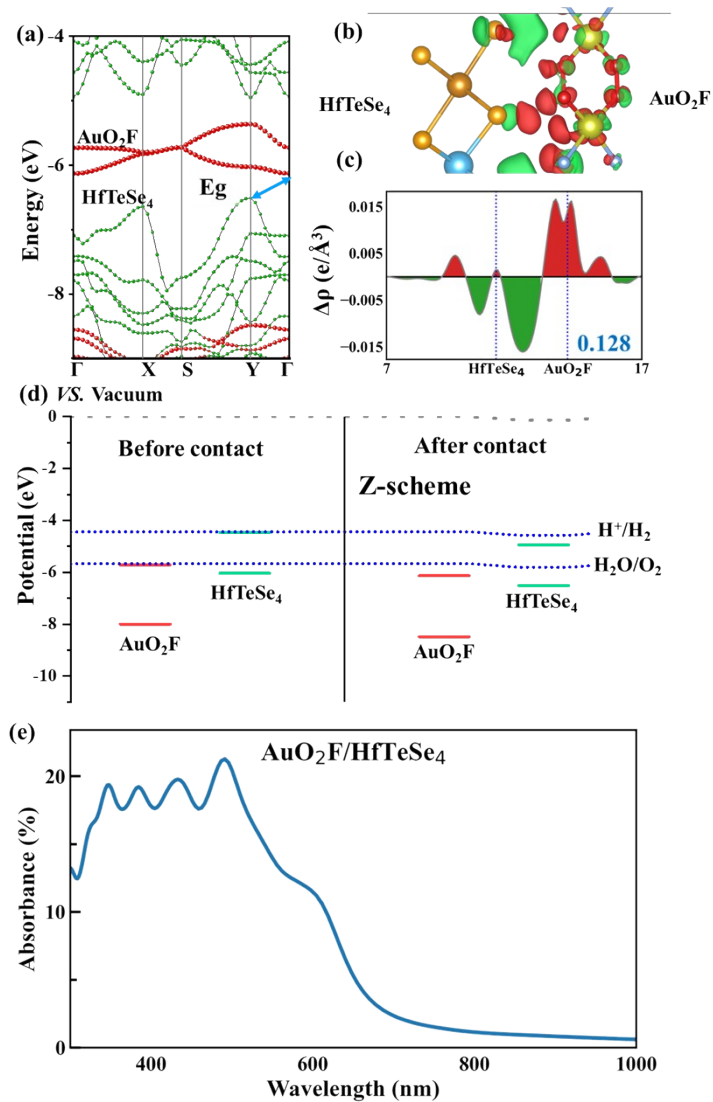


Figure S10. The electronic structures of $\text{AuO}_2\text{F}/\text{HfTeSe}_4$ were calculated, encompassing (a) HSE band structures, (b) charge transfer difference, (c) plane-integrated electron density difference along the vertical direction, (d) band alignment, and (e) absorption coefficients. The red and blue regions indicate electron accumulation and depletion, respectively. The isosurface value is $\pm 0.0002 \text{ e } \text{\AA}^{-3}$. The number labeled in blue is the amount of the interlayer charge transfer (in e) calculated by the Bader charge analysis.

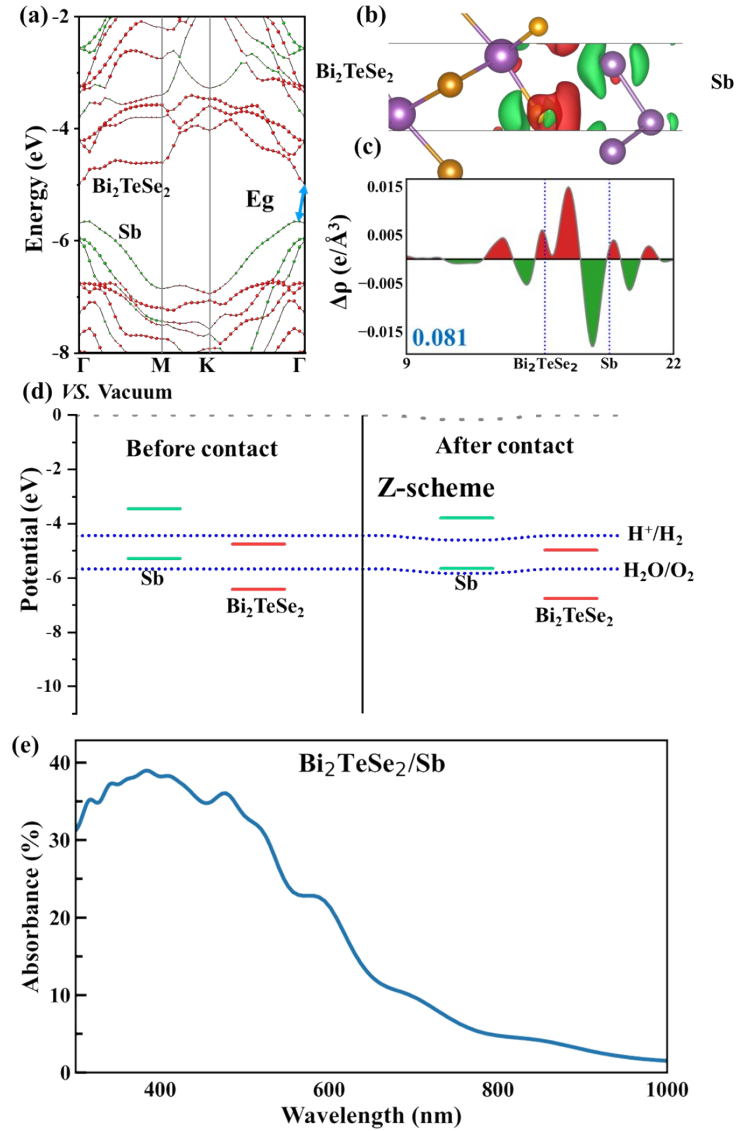


Figure S11. The electronic structures of $\text{Bi}_2\text{TeSe}_2/\text{Sb}$ were calculated, encompassing (a) HSE band structures, (b) charge transfer difference, (c) plane-integrated electron density difference along the vertical direction, (d) band alignment, and (e) absorption coefficients. The red and blue regions indicate electron accumulation and depletion, respectively. The isosurface value is $\pm 0.0002 \text{ e } \text{\AA}^{-3}$. The number labeled in blue is the amount of the interlayer charge transfer (in e) calculated by the Bader charge analysis.

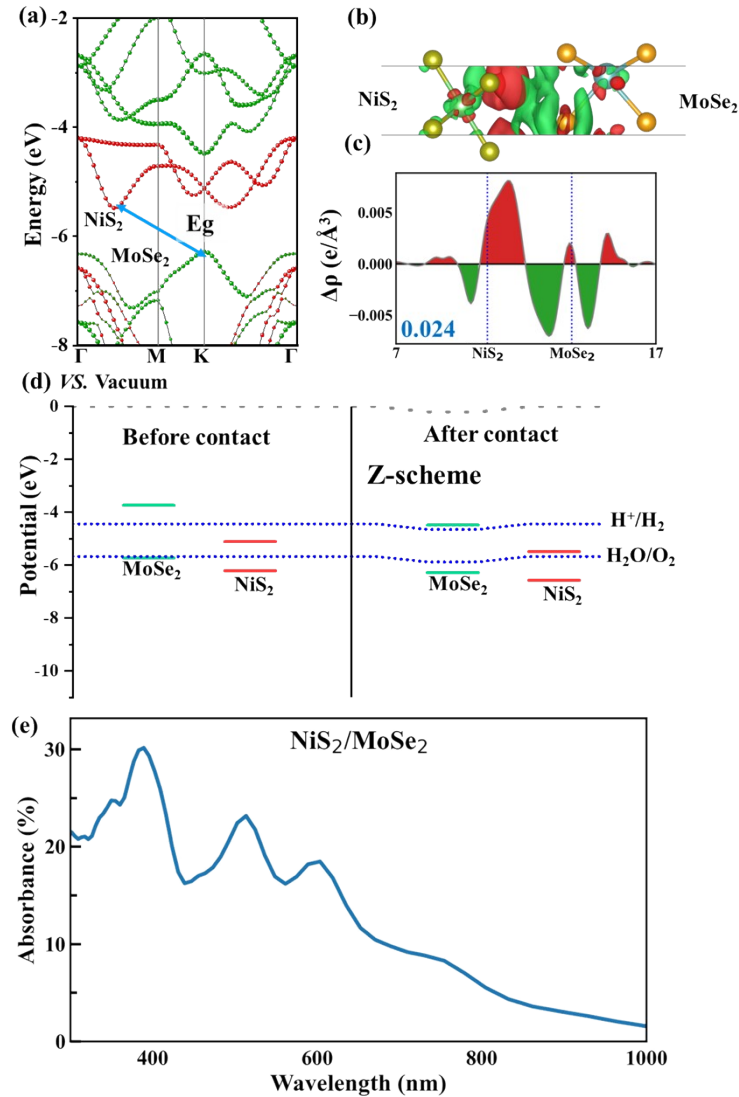


Figure S12. The electronic structures of NiS₂/MoSe₂ were calculated, encompassing (a) HSE band structures, (b) charge transfer difference, (c) plane-integrated electron density difference along the vertical direction, (d) band alignment, and (e) absorption coefficients. The red and blue regions indicate electron accumulation and depletion, respectively. The isosurface value is ± 0.0001 e Å⁻³. The number labeled in blue is the amount of the interlayer charge transfer (in e) calculated by the Bader charge analysis.

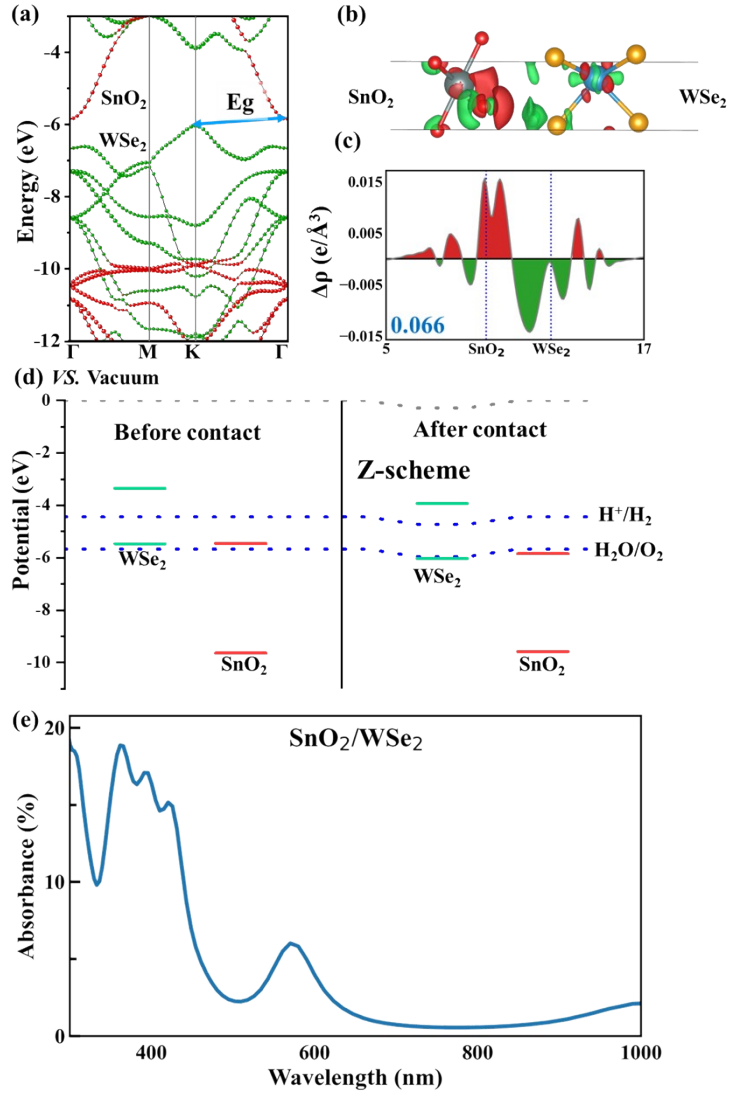


Figure S13. The electronic structures of $\text{SnO}_2/\text{WSe}_2$ were calculated, encompassing (a) HSE band structures, (b) charge transfer difference, (c) plane-integrated electron density difference along the vertical direction, (d) band alignment, and (e) absorption coefficients. The red and blue regions indicate electron accumulation and depletion, respectively. The isosurface value is $\pm 0.0003 \text{ e \AA}^{-3}$. The number labeled in blue is the amount of the interlayer charge transfer (in e) calculated by the Bader charge analysis.

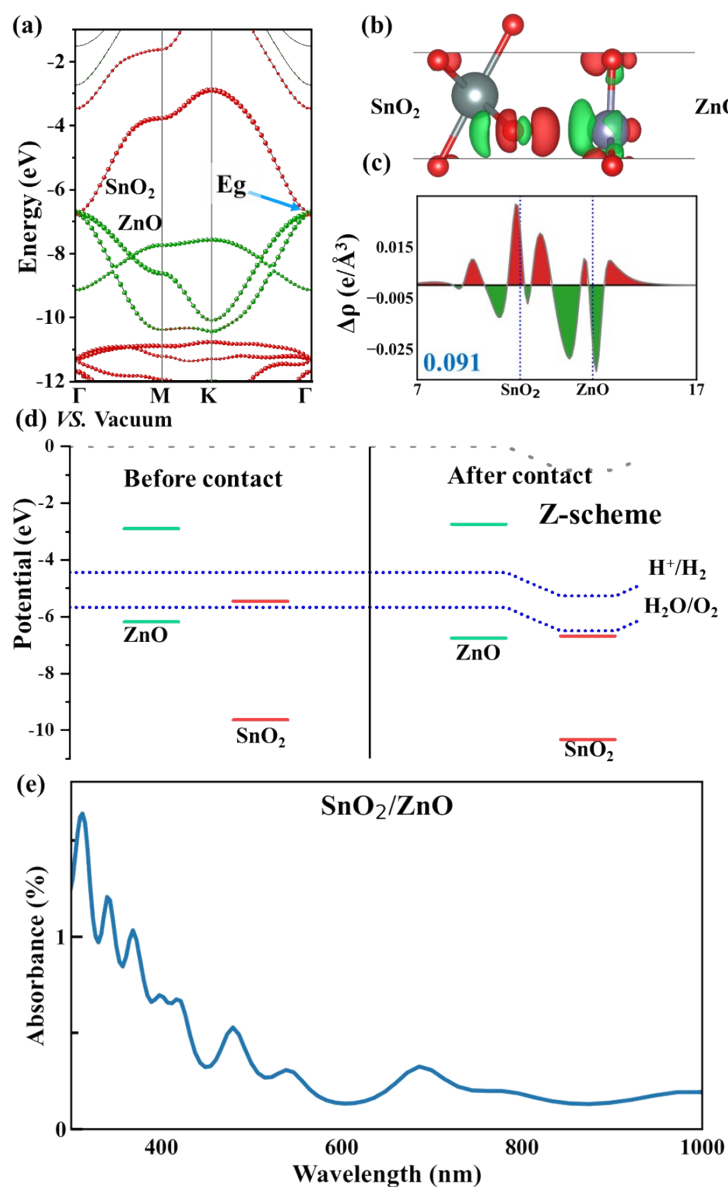


Figure S14. The electronic structures of SnO₂/ZnO were calculated, encompassing (a) HSE band structures, (b) charge transfer difference, (c) plane-integrated electron density difference along the vertical direction, (d) band alignment, and (e) absorption coefficients. The red and blue regions indicate electron accumulation and depletion, respectively. The isosurface value is $\pm 0.0008 \text{ e \AA}^{-3}$. The number labeled in blue is the amount of the interlayer charge transfer (in e) calculated by the Bader charge analysis.

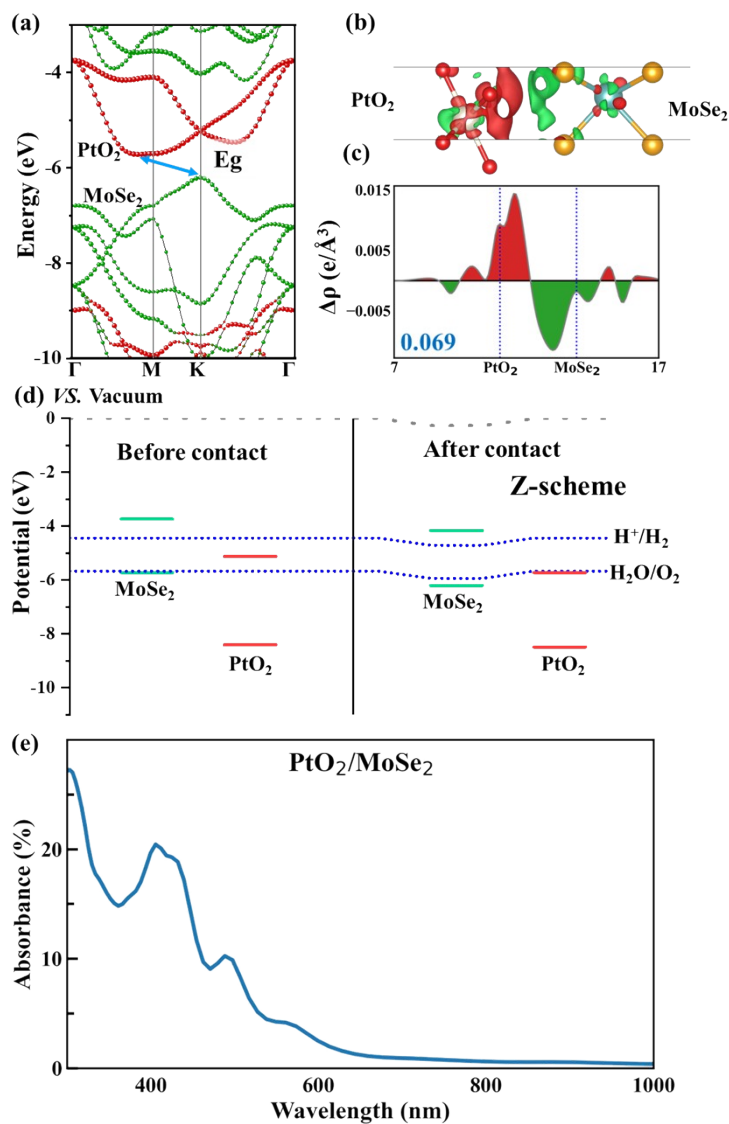


Figure S15. The electronic structures of PtO₂/MoSe₂ were calculated, encompassing (a) HSE band structures, (b) charge transfer difference, (c) plane-integrated electron density difference along the vertical direction, (d) band alignment, and (e) absorption coefficients. The red and blue regions indicate electron accumulation and depletion, respectively. The isosurface value is $\pm 0.0002 \text{ e \AA}^{-3}$. The number labeled in blue is the amount of the interlayer charge transfer (in e) calculated by the Bader charge analysis.

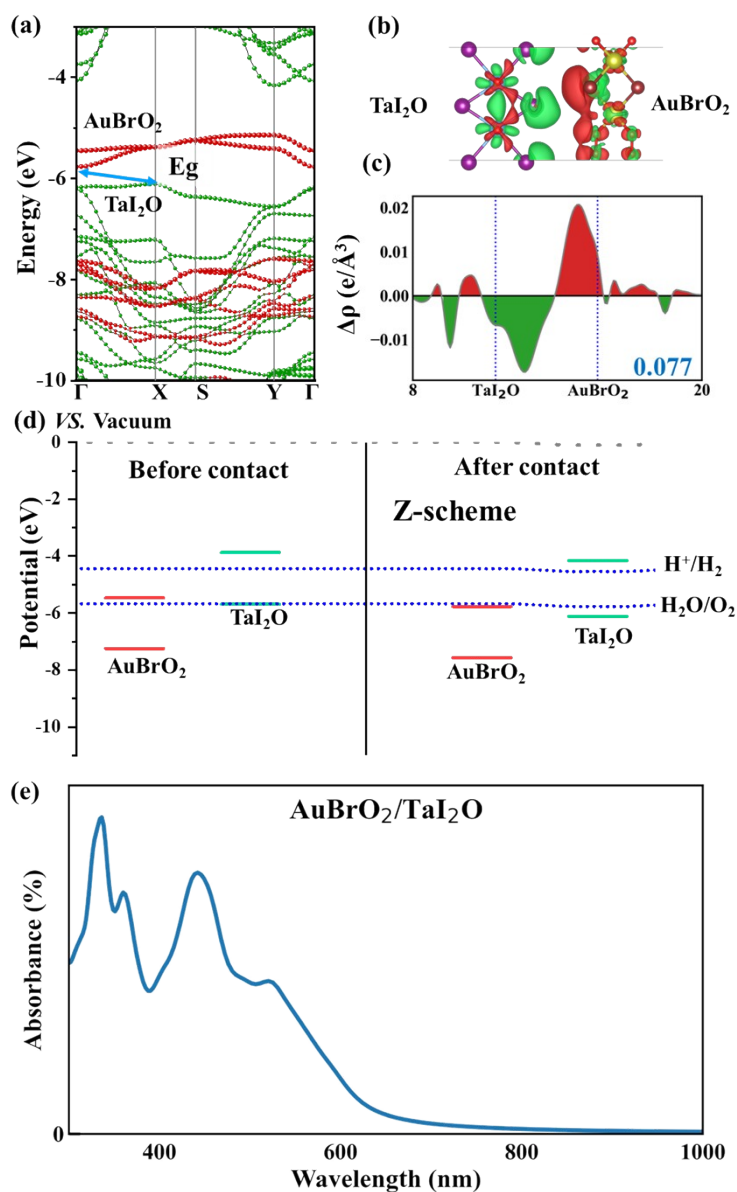


Figure S16. The electronic structures of AuBrO₂/TaI₂O were calculated, encompassing (a) HSE band structures, (b) charge transfer difference, (c) plane-integrated electron density difference along the vertical direction, (d) band alignment, and (e) absorption coefficients. The red and blue regions indicate electron accumulation and depletion, respectively. The isosurface value is $\pm 0.0001 \text{ e \AA}^{-3}$. The number labeled in blue is the amount of the interlayer charge transfer (in e) calculated by the Bader charge analysis.

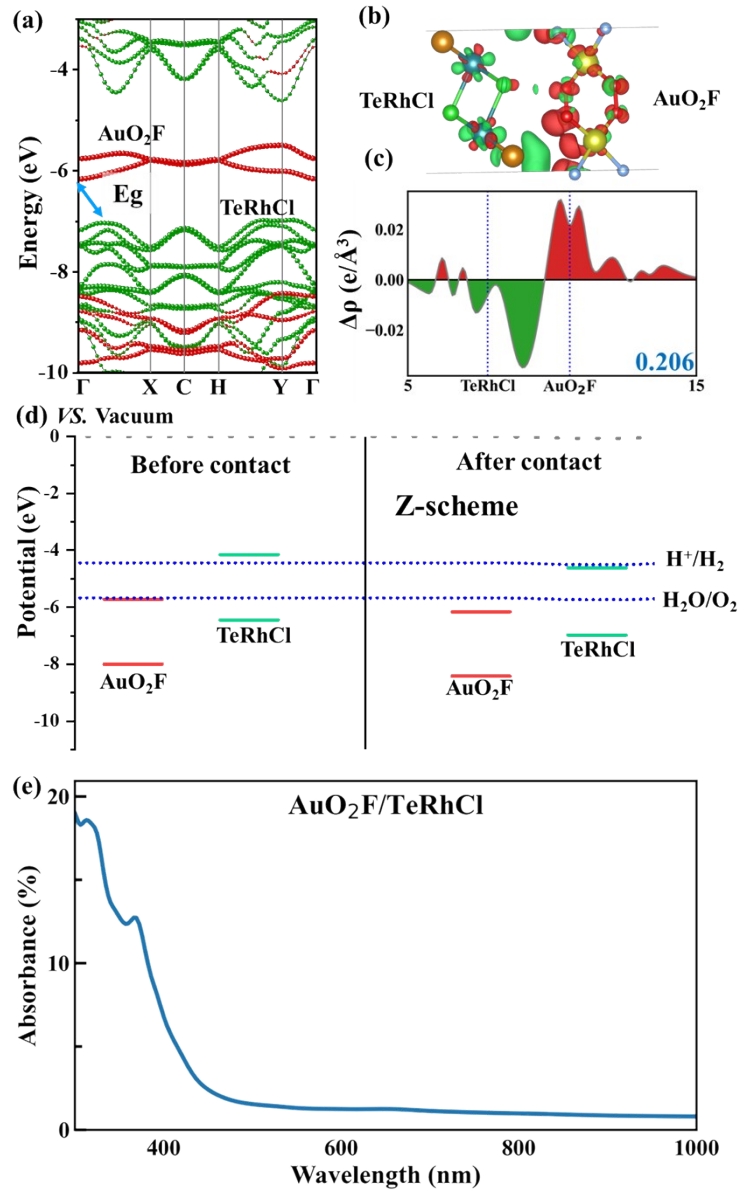


Figure S17. The electronic structures of $\text{AuO}_2\text{F}/\text{TeRhCl}$ were calculated, encompassing (a) HSE band structures, (b) charge transfer difference, (c) plane-integrated electron density difference along the vertical direction, (d) band alignment, and (e) absorption coefficients. The red and blue regions indicate electron accumulation and depletion, respectively. The isosurface value is $\pm 0.0004 \text{ e } \text{\AA}^{-3}$. The number labeled in blue is the amount of the interlayer charge transfer (in e) calculated by the Bader charge analysis.

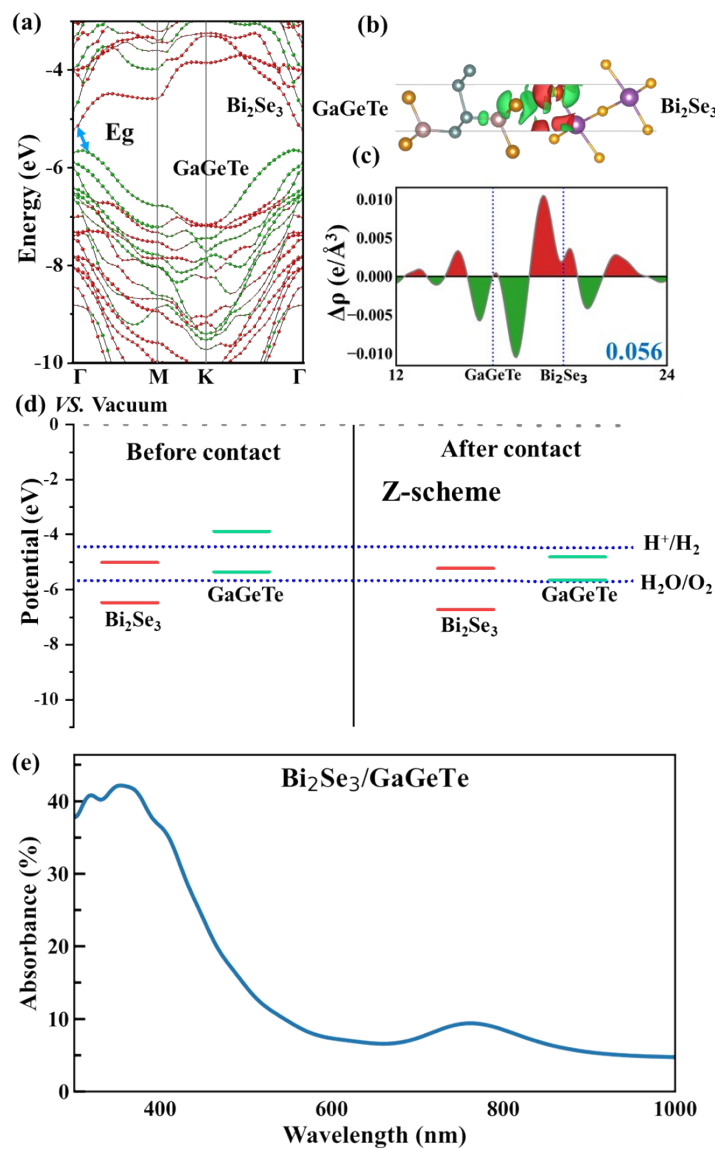


Figure S18. The electronic structures of $\text{Bi}_2\text{Se}_3/\text{GaTe}$ were calculated, encompassing (a) HSE band structures, (b) charge transfer difference, (c) plane-integrated electron density difference along the vertical direction, (d) band alignment, and (e) absorption coefficients. The red and blue regions indicate electron accumulation and depletion, respectively. The isosurface value is $\pm 0.0001 \text{ e } \text{\AA}^{-3}$. The number labeled in blue is the amount of the interlayer charge transfer (in e) calculated by the Bader charge analysis.

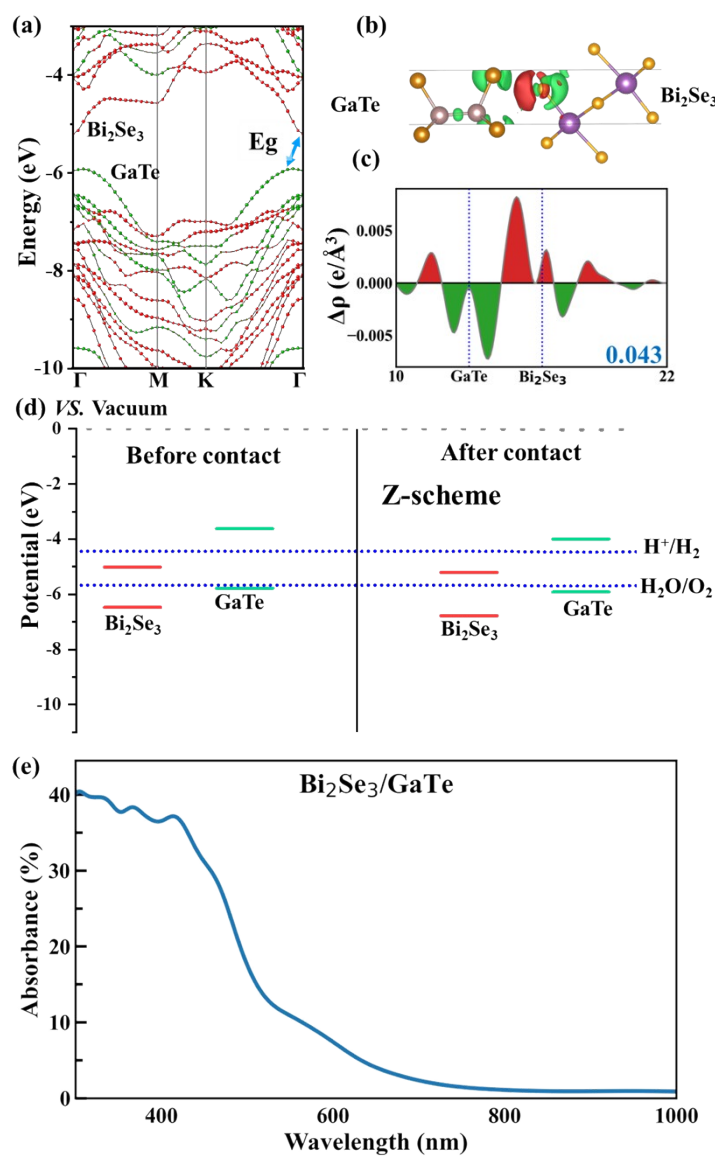


Figure S19. The electronic structures of $\text{Bi}_2\text{Se}_3/\text{GaTe}$ were calculated, encompassing (a) HSE band structures, (b) charge transfer difference, (c) plane-integrated electron density difference along the vertical direction, (d) band alignment, and (e) absorption coefficients. The red and blue regions indicate electron accumulation and depletion, respectively. The isosurface value is $\pm 0.0001 \text{ e \AA}^{-3}$. The number labeled in blue is the amount of the interlayer charge transfer (in e) calculated by the Bader charge analysis.

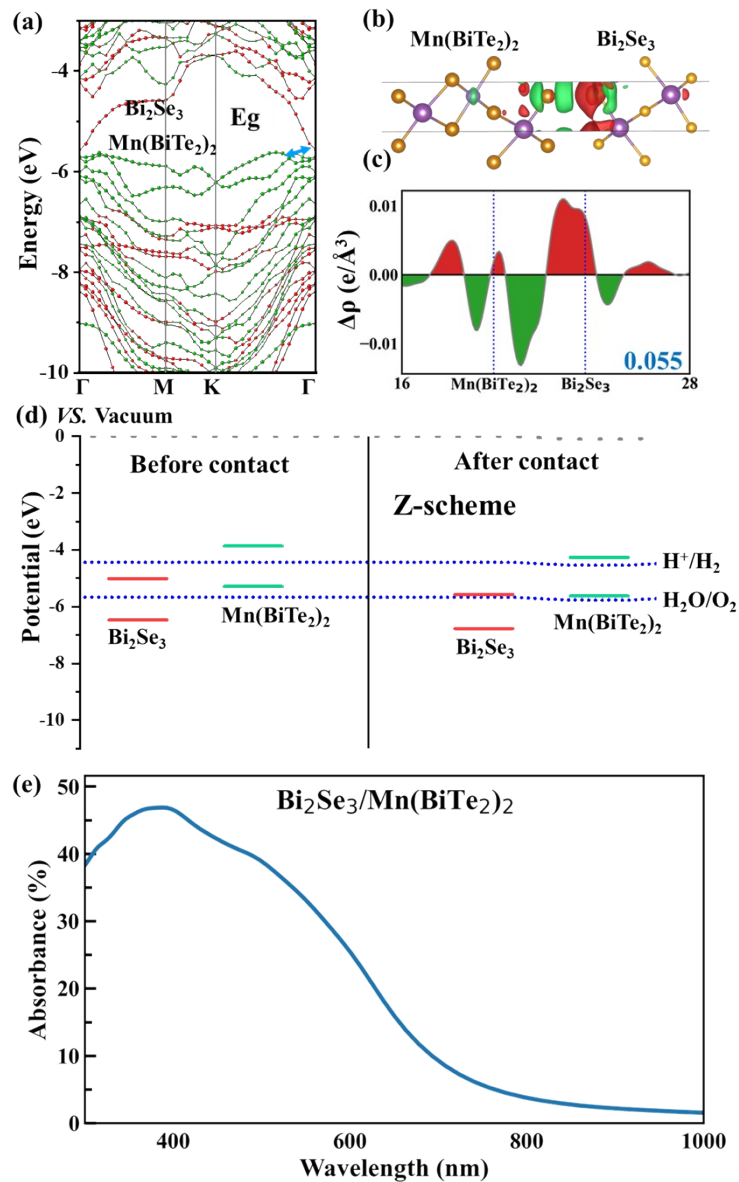


Figure S20. The electronic structures of $\text{Bi}_2\text{Se}_3/\text{Mn}(\text{BiTe}_2)_2$ were calculated, encompassing (a) HSE band structures (spin-up), (b) charge transfer difference, (c) plane-integrated electron density difference along the vertical direction, (d) band alignment, and (e) absorption coefficients. The red and blue regions indicate electron accumulation and depletion, respectively. The isosurface value is $\pm 0.0001 \text{ e \AA}^{-3}$. The number labeled in blue is the amount of the interlayer charge transfer (in e) calculated by the Bader charge analysis.

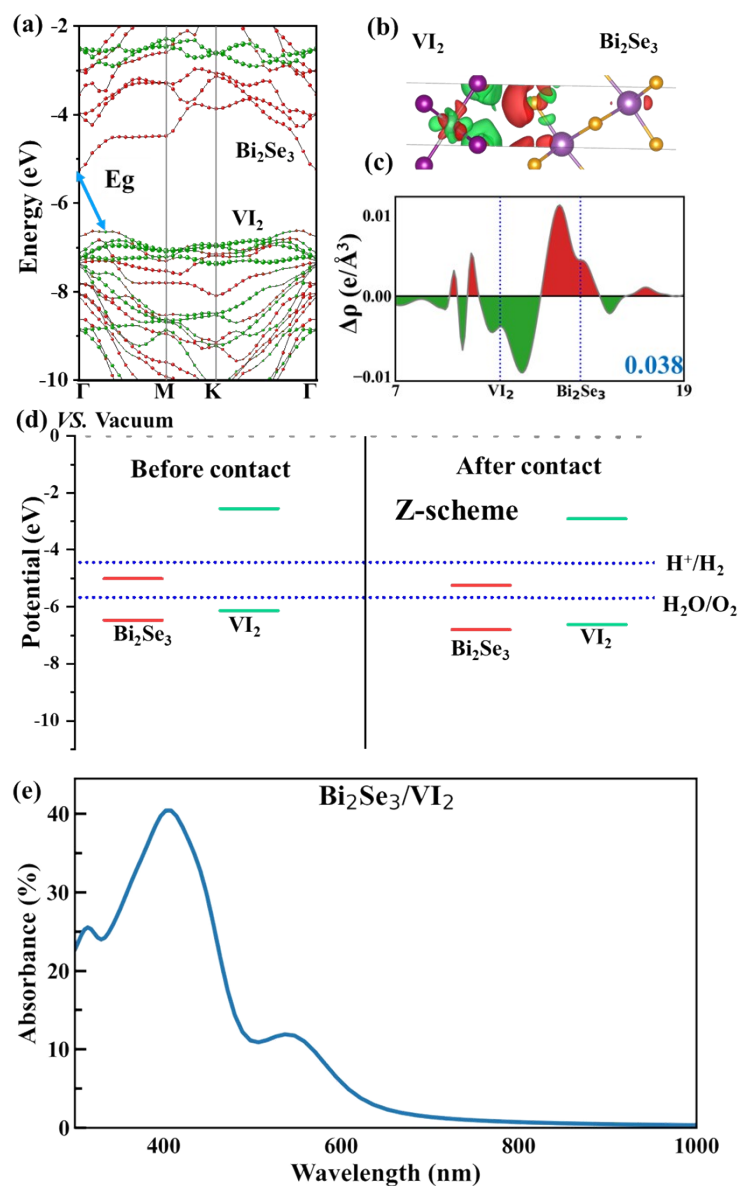


Figure S21. The electronic structures of $\text{Bi}_2\text{Se}_3/\text{VI}_2$ were calculated, encompassing (a) HSE band structures (spin-up), (b) charge transfer difference, (c) plane-integrated electron density difference along the vertical direction, (d) band alignment, and (e) absorption coefficients. The red and blue regions indicate electron accumulation and depletion, respectively. The isosurface value is $\pm 0.0001 \text{ e \AA}^{-3}$. The number labeled in blue is the amount of the interlayer charge transfer (in e) calculated by the Bader charge analysis.

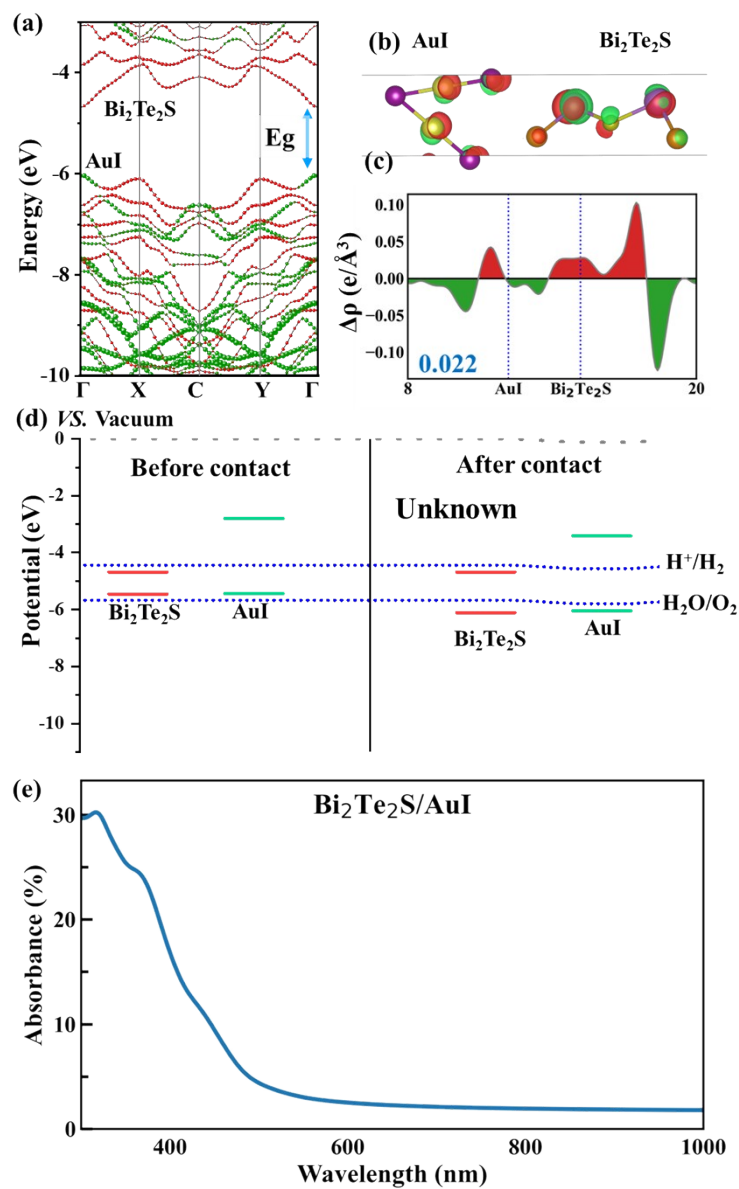


Figure S22. The electronic structures of $\text{Bi}_2\text{Te}_2\text{S}/\text{AuI}$ were calculated, encompassing (a) HSE band structures, (b) charge transfer difference, (c) plane-integrated electron density difference along the vertical direction, (d) band alignment, and (e) absorption coefficients. The red and blue regions indicate electron accumulation and depletion, respectively. The isosurface value is $\pm 0.0003 \text{ e \AA}^{-3}$. The number labeled in blue is the amount of the interlayer charge transfer (in e) calculated by the Bader charge analysis.

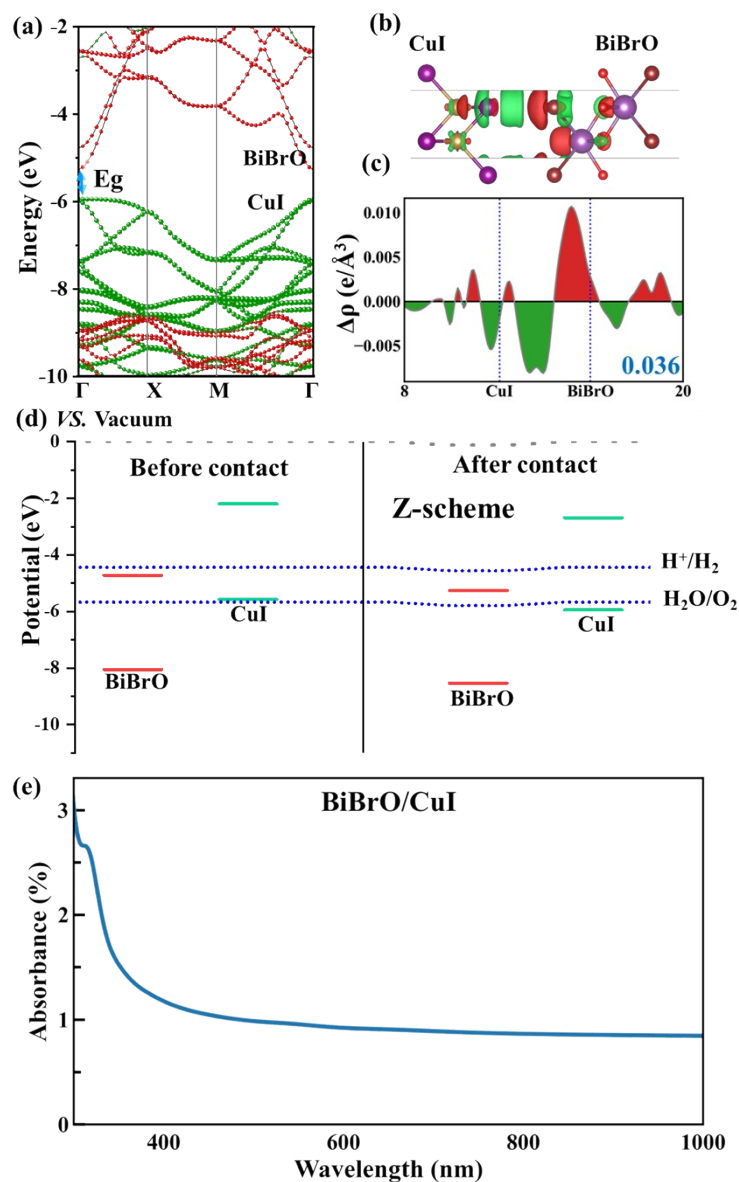


Figure S23. The electronic structures of BiBrO/CuI were calculated, encompassing (a) HSE band structures, (b) charge transfer difference, (c) plane-integrated electron density difference along the vertical direction, (d) band alignment, and (e) absorption coefficients. The red and blue regions indicate electron accumulation and depletion, respectively. The isosurface value is $\pm 0.0001 \text{ e \AA}^{-3}$. The number labeled in blue is the amount of the interlayer charge transfer (in e) calculated by the Bader charge analysis.

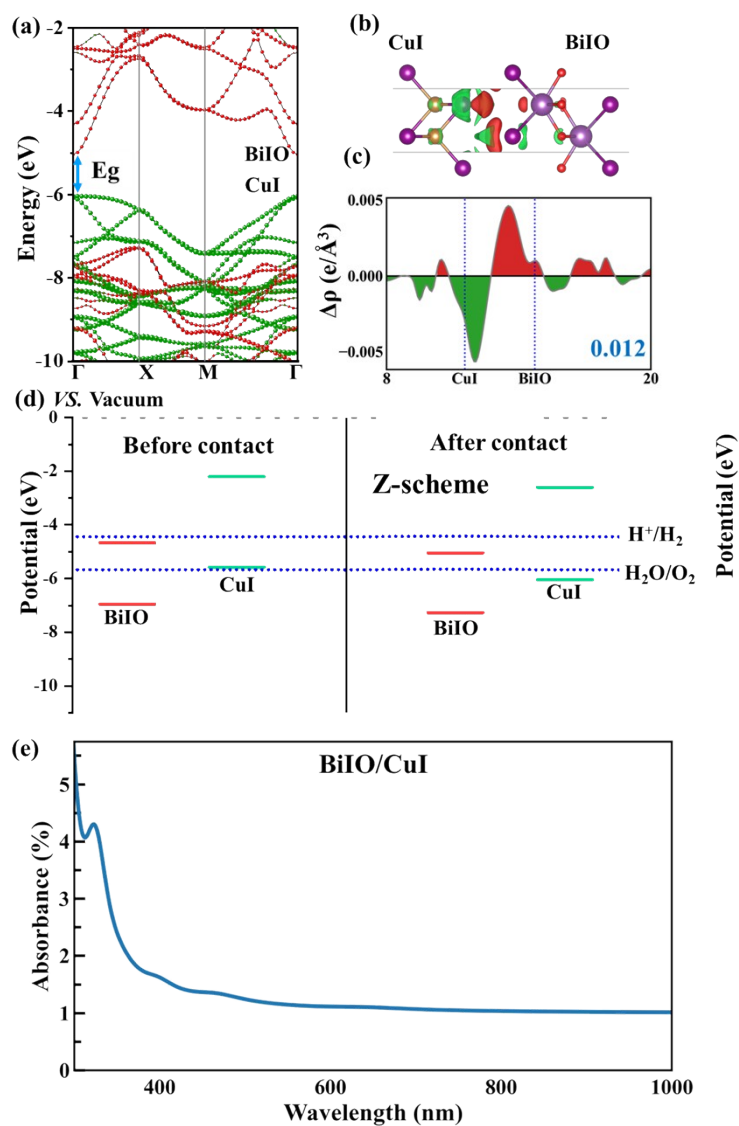


Figure S24. The electronic structures of BiIO/CuI were calculated, encompassing (a) HSE band structures, (b) charge transfer difference, (c) plane-integrated electron density difference along the vertical direction, (d) band alignment, and (e) absorption coefficients. The red and blue regions indicate electron accumulation and depletion, respectively. The isosurface value is $\pm 0.0001 \text{ e \AA}^{-3}$. The number labeled in blue is the amount of the interlayer charge transfer (in e) calculated by the Bader charge analysis.

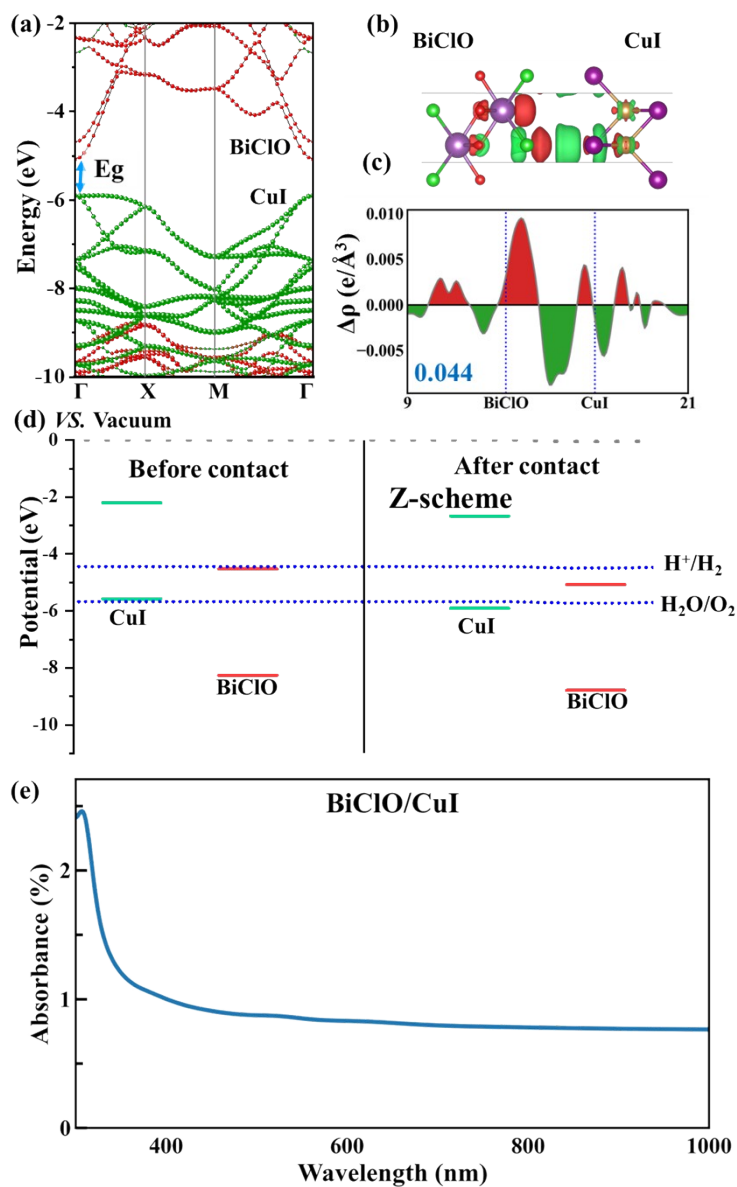


Figure S25. The electronic structures of BiClO/CuI were calculated, encompassing (a) HSE band structures, (b) charge transfer difference, (c) plane-integrated electron density difference along the vertical direction, (d) band alignment, and (e) absorption coefficients. The red and blue regions indicate electron accumulation and depletion, respectively. The isosurface value is $\pm 0.0001 \text{ e \AA}^{-3}$. The number labeled in blue is the amount of the interlayer charge transfer (in e) calculated by the Bader charge analysis.

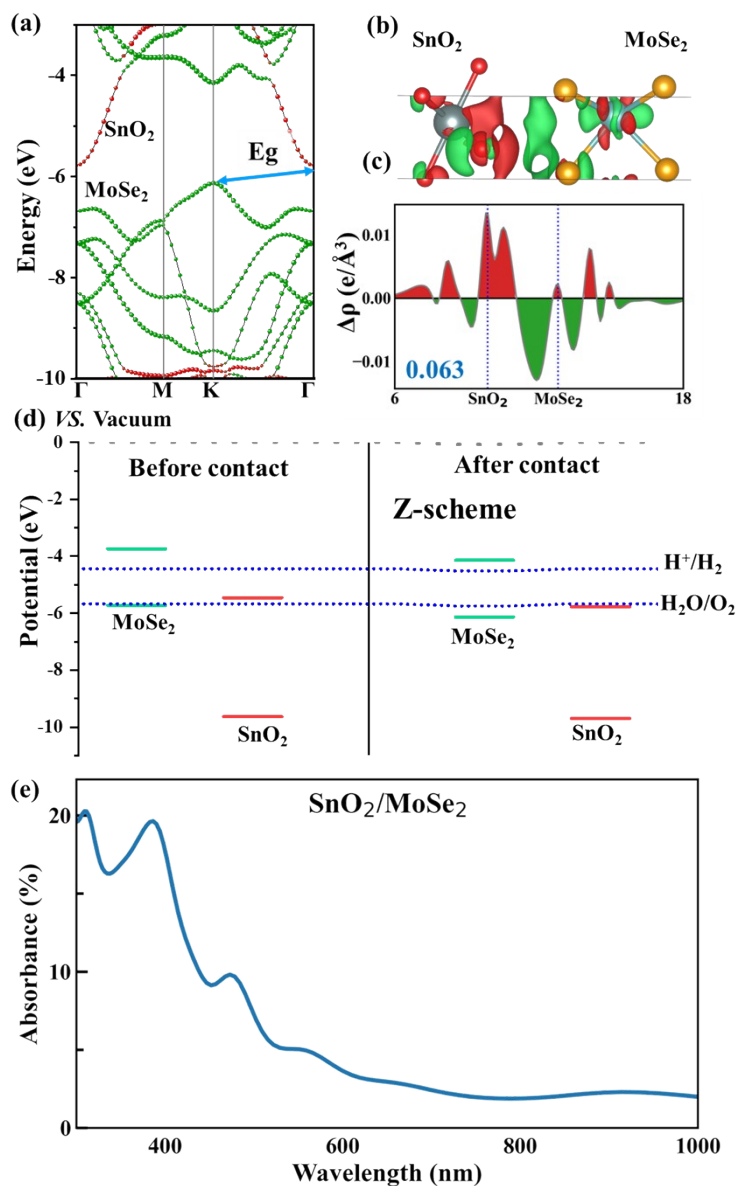


Figure S26. The electronic structures of SnO₂/MoSe₂ were calculated, encompassing (a) HSE band structures, (b) charge transfer difference, (c) plane-integrated electron density difference along the vertical direction, (d) band alignment, and (e) absorption coefficients. The red and blue regions indicate electron accumulation and depletion, respectively. The isosurface value is $\pm 0.0002 \text{ e \AA}^{-3}$. The number labeled in blue is the amount of the interlayer charge transfer (in e) calculated by the Bader charge analysis.

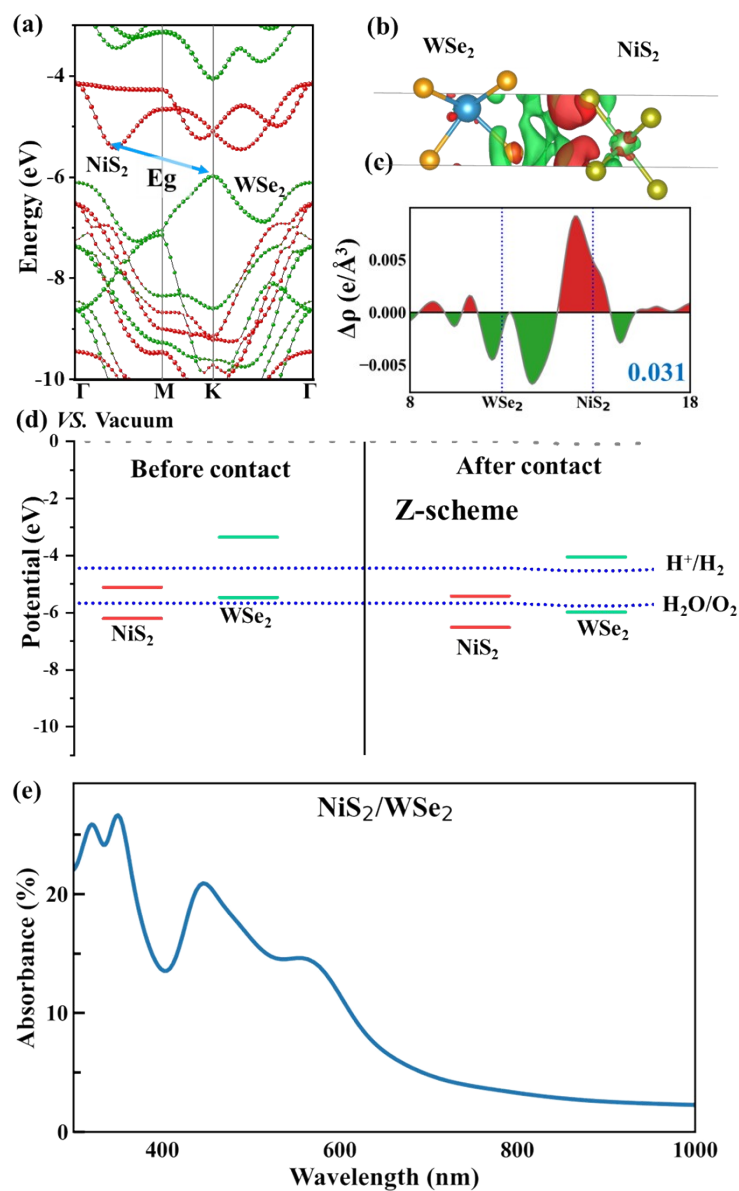


Figure S27. The electronic structures of NiS₂/WSe₂ were calculated, encompassing (a) HSE band structures, (b) charge transfer difference, (c) plane-integrated electron density difference along the vertical direction, (d) band alignment, and (e) absorption coefficients. The red and blue regions indicate electron accumulation and depletion, respectively. The isosurface value is $\pm 0.0001 \text{ e \AA}^{-3}$. The number labeled in blue is the amount of the interlayer charge transfer (in e) calculated by the Bader charge analysis.

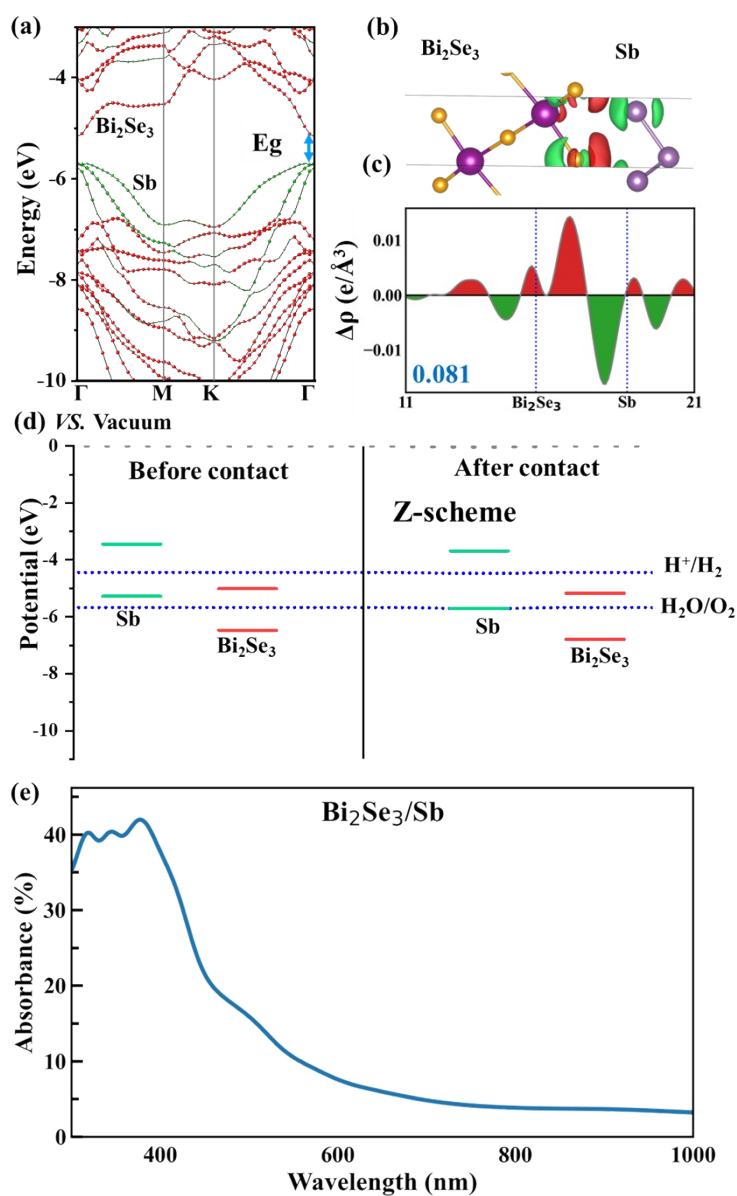


Figure S28. The electronic structures of $\text{Bi}_2\text{Se}_3/\text{Sb}$ were calculated, encompassing (a) HSE band structures, (b) charge transfer difference, (c) plane-integrated electron density difference along the vertical direction, (d) band alignment, and (e) absorption coefficients. The red and blue regions indicate electron accumulation and depletion, respectively. The isosurface value is $\pm 0.0002 \text{ e \AA}^{-3}$. The number labeled in blue is the amount of the interlayer charge transfer (in e) calculated by the Bader charge analysis.

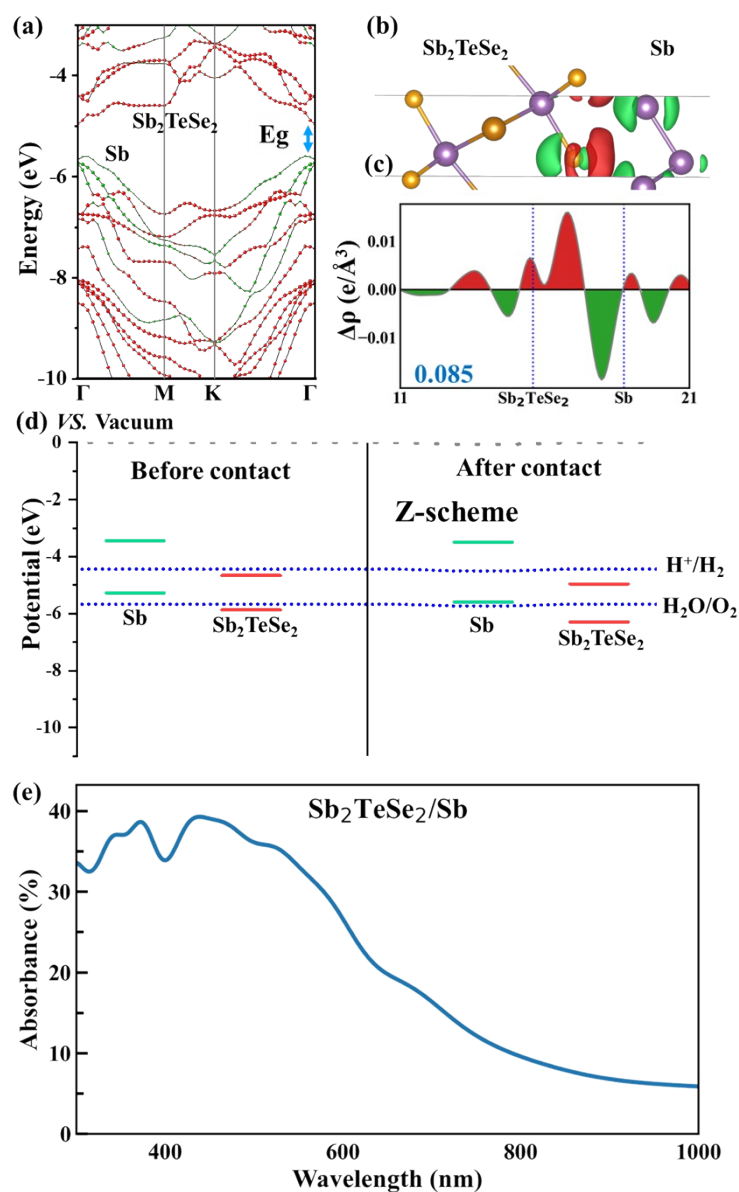


Figure S29. The electronic structures of $\text{Sb}_2\text{TeSe}_2/\text{Sb}$ were calculated, encompassing (a) HSE band structures, (b) charge transfer difference, (c) plane-integrated electron density difference along the vertical direction, (d) band alignment, and (e) absorption coefficients. The red and blue regions indicate electron accumulation and depletion, respectively. The isosurface value is $\pm 0.0002 \text{ e \AA}^{-3}$. The number labeled in blue is the amount of the interlayer charge transfer (in e) calculated by the Bader charge analysis.

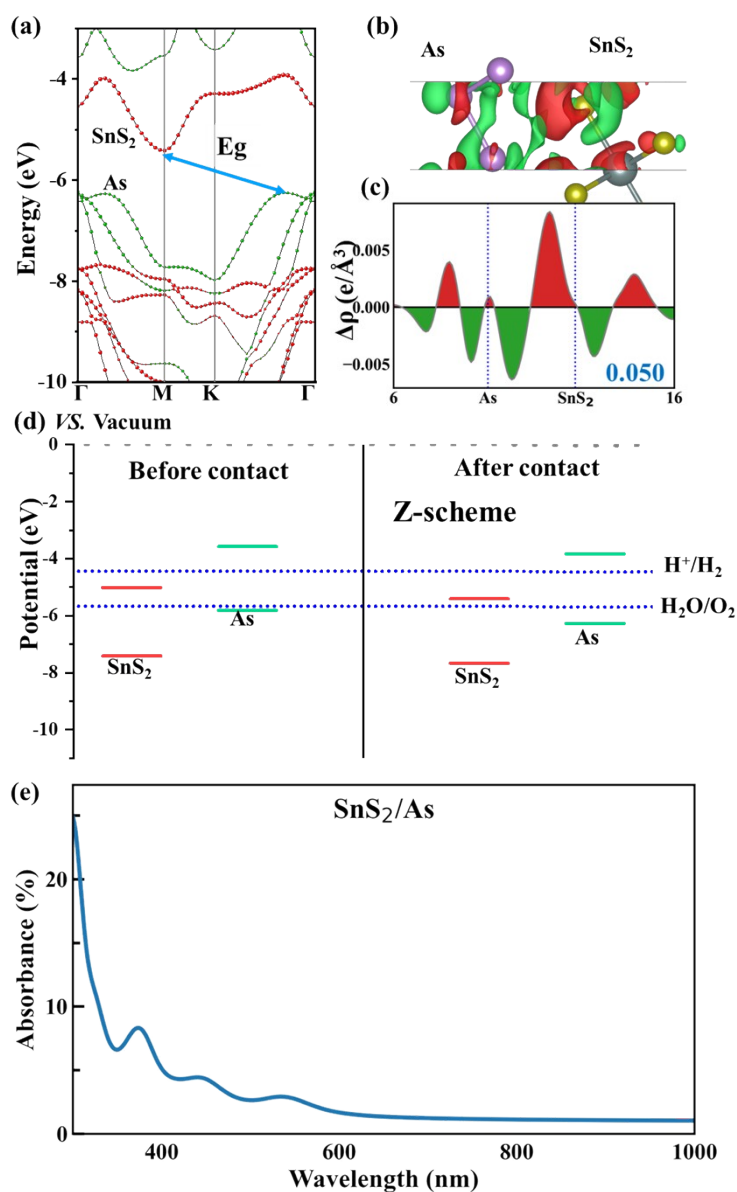


Figure S30. The electronic structures of SnS₂/As were calculated, encompassing (a) HSE band structures, (b) charge transfer difference, (c) plane-integrated electron density difference along the vertical direction, (d) band alignment, and (e) absorption coefficients. The red and blue regions indicate electron accumulation and depletion, respectively. The isosurface value is $\pm 0.0001 \text{ e \AA}^{-3}$. The number labeled in blue is the amount of the interlayer charge transfer (in e) calculated by the Bader charge analysis.

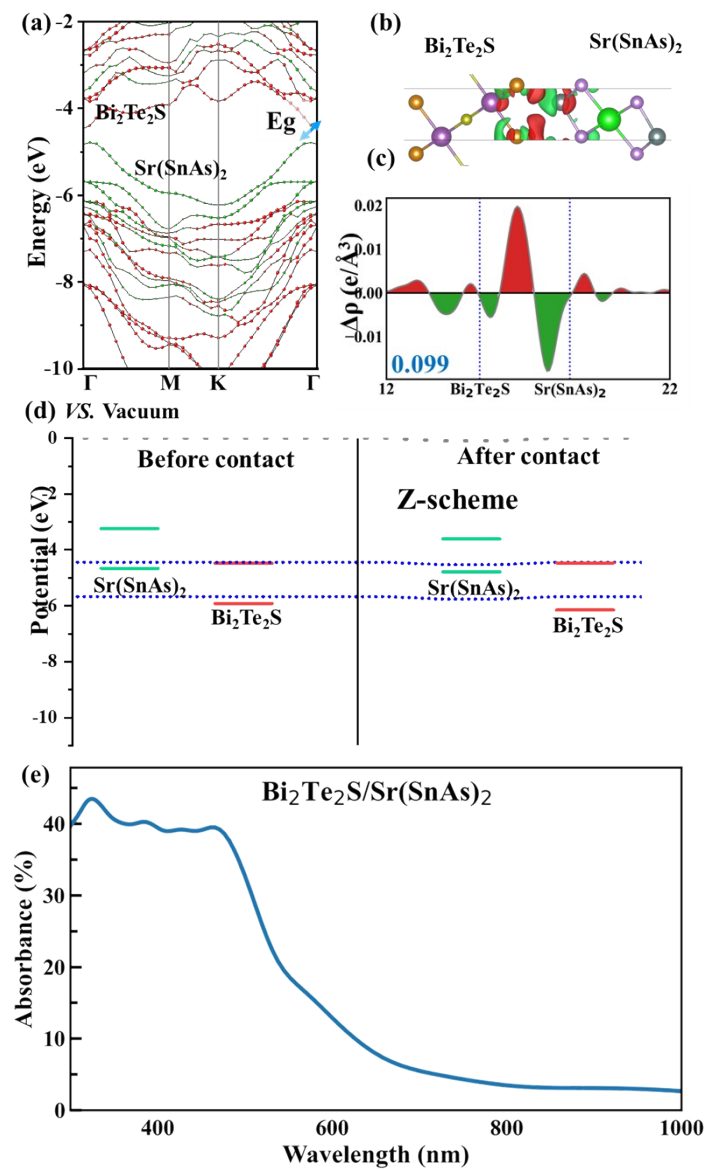


Figure S31. The electronic structures of $\text{Bi}_2\text{Te}_2\text{S}/\text{Sr}(\text{SnAs})_2$ were calculated, encompassing (a) HSE band structures, (b) charge transfer difference, (c) plane-integrated electron density difference along the vertical direction, (d) band alignment, and (e) absorption coefficients. The red and blue regions indicate electron accumulation and depletion, respectively. The isosurface value is $\pm 0.0002 \text{ e } \text{\AA}^{-3}$. The number labeled in blue is the amount of the interlayer charge transfer (in e) calculated by the Bader charge analysis.

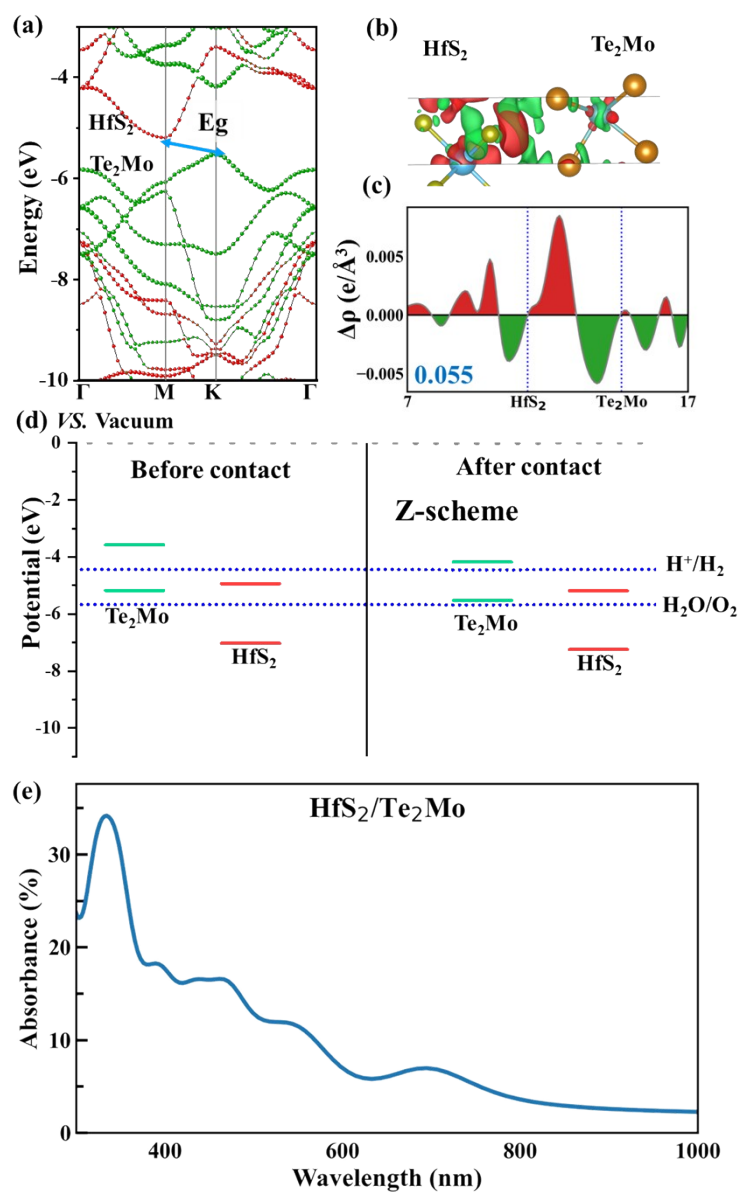


Figure S32. The electronic structures of $\text{HfS}_2/\text{Te}_2\text{Mo}$ were calculated, encompassing (a) HSE band structures, (b) charge transfer difference, (c) plane-integrated electron density difference along the vertical direction, (d) band alignment, and (e) absorption coefficients. The red and blue regions indicate electron accumulation and depletion, respectively. The isosurface value is $\pm 0.0001 \text{ e \AA}^{-3}$. The number labeled in blue is the amount of the interlayer charge transfer (in e) calculated by the Bader charge analysis.

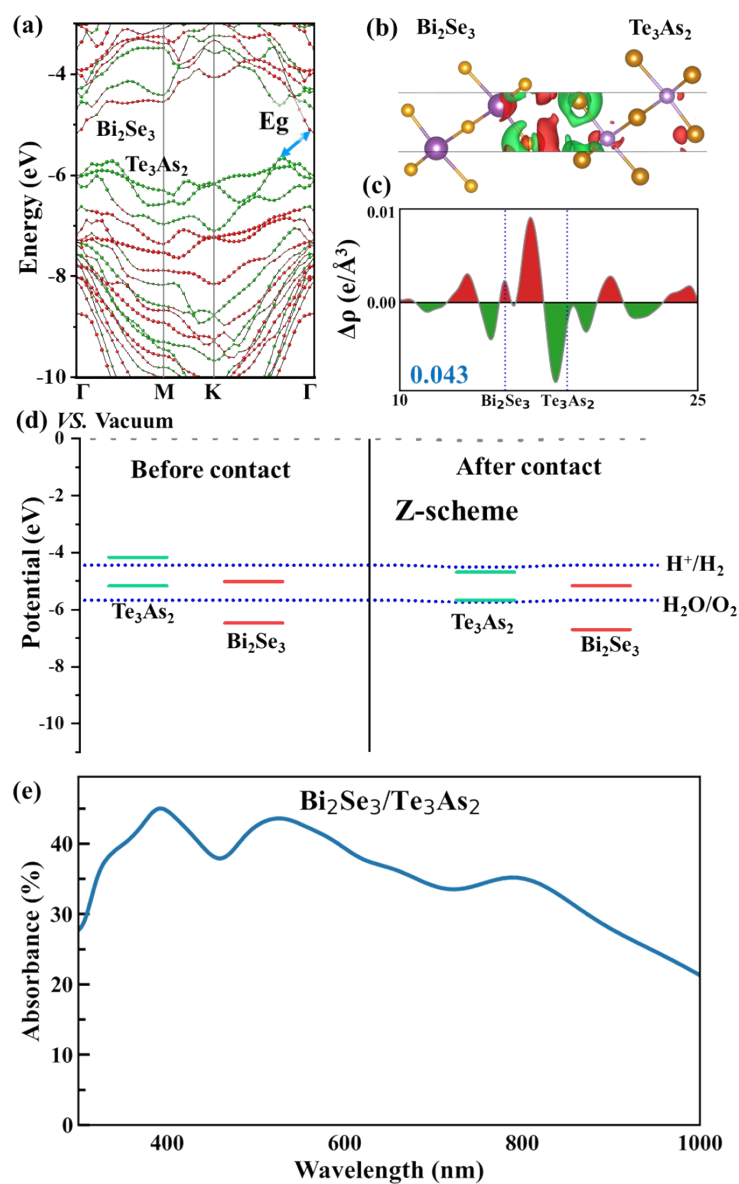


Figure S33. The electronic structures of $\text{Bi}_2\text{Se}_3/\text{Te}_3\text{As}_2$ were calculated, encompassing (a) HSE band structures, (b) charge transfer difference, (c) plane-integrated electron density difference along the vertical direction, (d) band alignment, and (e) absorption coefficients. The red and blue regions indicate electron accumulation and depletion, respectively. The isosurface value is $\pm 0.0003 \text{ e \AA}^{-3}$. The number labeled in blue is the amount of the interlayer charge transfer (in e) calculated by the Bader charge analysis.

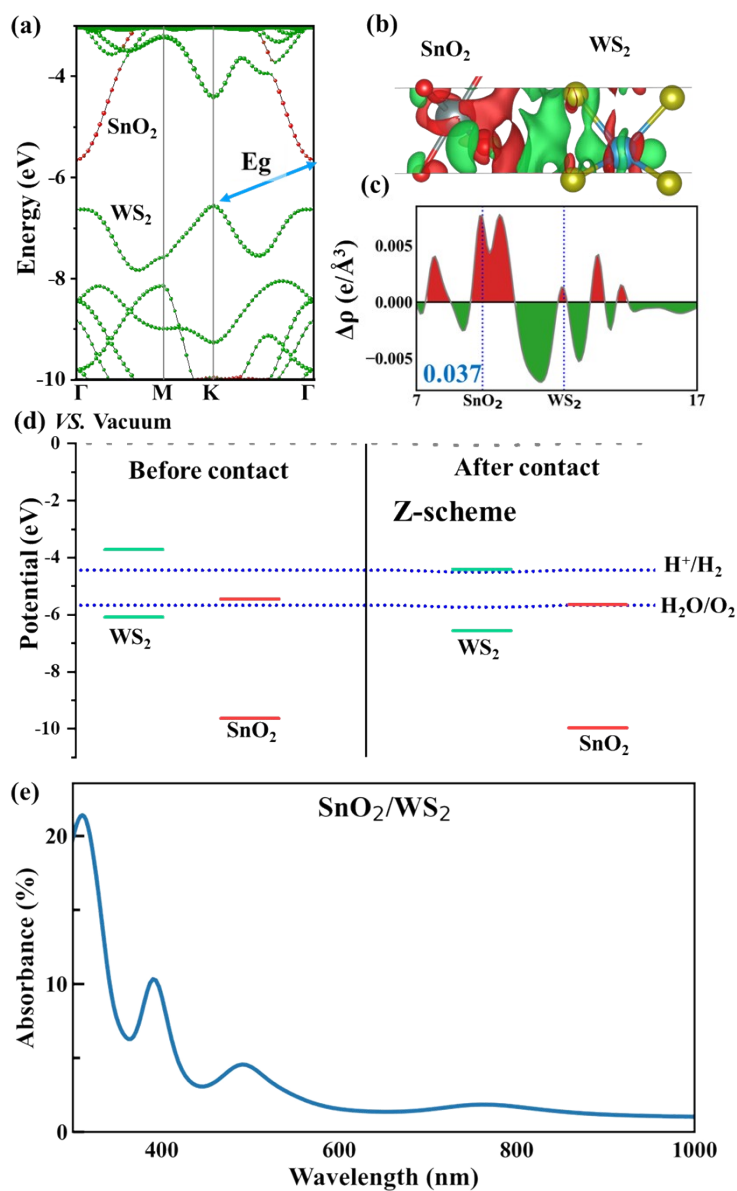


Figure S34. The electronic structures of SnO₂/WS₂ were calculated, encompassing (a) HSE band structures, (b) charge transfer difference, (c) plane-integrated electron density difference along the vertical direction, (d) band alignment, and (e) absorption coefficients. The red and blue regions indicate electron accumulation and depletion, respectively. The isosurface value is $\pm 0.0001 \text{ e \AA}^{-3}$. The number labeled in blue is the amount of the interlayer charge transfer (in e) calculated by the Bader charge analysis.

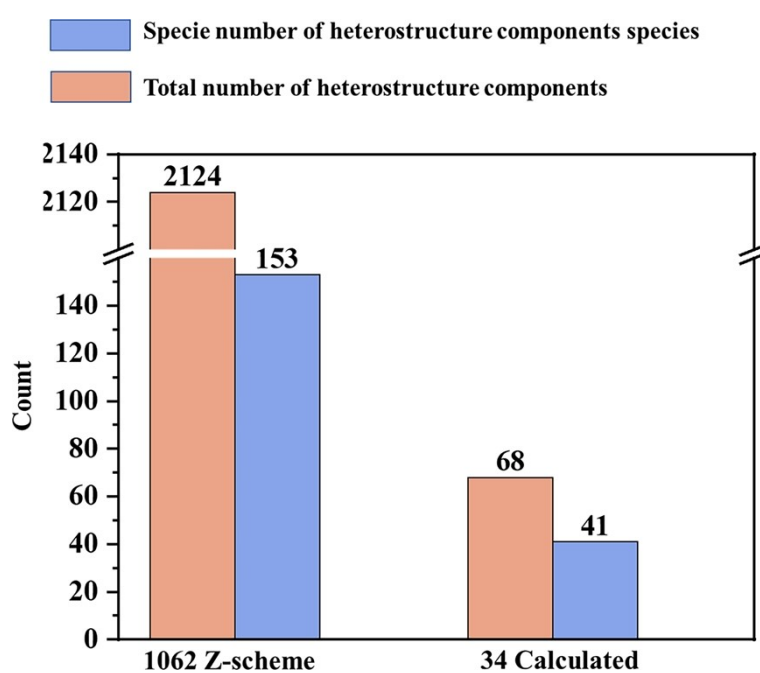


Figure S35. Histograms of materials species and materials number

References

1. J. Zhou, L. Shen, M. D. Costa, K. A. Persson, S. P. Ong, P. Huck, Y. Lu, X. Ma,

- Y. Chen, H. Tang and Y. P. Feng, *Scientific Data*, 2019, **6**, 86.
2. L. C. Allen, *Journal of the American Chemical Society*, 1989, **111**, 9003-9014.
 3. J. B. Mann, T. L. Meek and L. C. Allen, *Journal of the American Chemical Society*, 2000, **122**, 2780-2783.
 4. J. B. Mann, T. L. Meek, E. T. Knight, J. F. Capitani and L. C. Allen, *Journal of the American Chemical Society*, 2000, **122**, 5132-5137.
 5. X. Liu, Y.-M. Zhao, X. Zhang, L. Wang, J. Shen, M. Zhou and L. Shen, *ACS Catalysis*, 2023, DOI: 10.1021/acscatal.3c02315, 9936-9945.
 6. A. L. Allred and E. G. Rochow, *Journal of Inorganic and Nuclear Chemistry*, 1958, **5**, 264-268.
 7. W. Tenachi, R. Ibata and F. I. Diakogiannis, *arXiv preprint arXiv:2303.03192*, 2023.
 8. G. E. Hinton, S. Osindero and Y.-W. Teh, *Neural Comput.*, 2006, **18**, 1527-1554.
 9. V. Nair and G. E. Hinton, 2010.
 10. N. Srivastava, G. Hinton, A. Krizhevsky, I. Sutskever and R. Salakhutdinov, *The journal of machine learning research*, 2014, **15**, 1929-1958.
 11. D. P. Kingma, *arXiv preprint arXiv:1412.6980*, 2014.
 12. C. M. Bishop and N. M. Nasrabadi, *Pattern recognition and machine learning*, Springer, 2006.
 13. S. P. Ong, W. D. Richards, A. Jain, G. Hautier, M. Kocher, S. Cholia, D. Gunter, V. L. Chevrier, K. A. Persson and G. Ceder, *Computational Materials Science*, 2013, **68**, 314-319.
 14. A. Jain, S. P. Ong, G. Hautier, W. Chen, W. D. Richards, S. Dacek, S. Cholia, D. Gunter, D. Skinner, G. Ceder and K. A. Persson, *APL Materials*, 2013, **1**, 011002.
 15. I. Goodfellow, *Journal*, 2016.
 16. A. Karpatne, G. Atluri, J. H. Faghmous, M. Steinbach, A. Banerjee, A. Ganguly, S. Shekhar, N. Samatova and V. Kumar, *IEEE Transactions on Knowledge and Data Engineering*, 2017, **29**, 2318-2331.
 17. J. W. Cort and M. Kenji, *Clim. Res.*, 2005, **30**, 79-82.
 18. H. Razavi-Khosroshahi, K. Edalati, J. Wu, Y. Nakashima, M. Arita, Y. Ikoma, M. Sadakiyo, Y. Inagaki, A. Staykov, M. Yamauchi, Z. Horita and M. Fuji, *Journal of Materials Chemistry A*, 2017, **5**, 20298-20303.
 19. X. Liu, W. Kang, L. Qi, J. Zhao, Y. Wang, L. Wang, W. Wang, L. Fang and M. Zhou, *Physica E: Low-dimensional Systems and Nanostructures*, 2021, 114872.
 20. C. Cheng, B. He, J. Fan, B. Cheng, S. Cao and J. Yu, *Adv. Mater.*, 2021, **33**, 2100317.
 21. L. Zhao, B. Yang, G. Zhuang, Y. Wen, T. Zhang, M. Lin, Z. Zhuang and Y. Yu, *Small*, 2022, **18**, 2201668.
 22. C.-F. Fu, R. Zhang, Q. Luo, X. Li and J. Yang, *J. Comput. Chem.*, 2019, **40**, 980-987.
 23. X. H. H. H. Z. J. Yang Liu, *Acta Physico-Chimica Sinica*, 2021, **37**, 2008030.
 24. Y. Yu, B. Yao, B. Cao and W. Ma, *Photochemistry and Photobiology*, 2019, **95**, 1131-1141.

25. X. Gao, Y. Shen, J. Liu, L. Lv, M. Zhou, Z. Zhou, Y. P. Feng and L. Shen, *Catalysis Science & Technology*, 2022, **12**, 3614-3621.
26. S.-m. Tian, J. Meng, J. Huang and Q.-x. Li, *Chin. J. Chem. Phys.*, 2020, **33**, 427-433.
27. B. Liu, X. Hu, J. Yang, C. Yang and Y. Huang, *Catalysis Science & Technology*, 2023, **13**, 504-515.
28. X. Yang, X. Qin, J. Luo, N. Abbas, J. Tang, Y. Li and K. Gu, *RSC Advances*, 2020, **10**, 2615-2623.